Colloidal synthesis of high entropy alloy and multimetallic nanocrystals

Jinwon Oh,[1] Shuang Han,[2] Evan J. Gardner,[3] Rohan Parekh,[1] Audrey Dannar,[4] Pin-Hung Chung,[1] Kaifeng Zheng,[5] Anna Mian,[6] Karen C. Bustillo,[7] Christian Reece,[4] Anatoly I. Frenkel,[5, 8] Colin Ophus,[1] Carlos Lizandara-Pueyo,[2,9] Sandip De,[2, *] Matteo Cargnello[3, *]

[1]*Department of Materials Science and Engineering, Stanford University, Stanford, CA 94305, USA*

[2]*BASF SE, Carl-Bosch-Straße 38, 67056, Ludwigshafen, Germany*

[3]*Department of Chemical Engineering and SUNCAT Center for Interface Science and Catalysis, Stanford University, Stanford, CA 94305, USA*

[4]*Rowland Institute at Harvard, Harvard University, Cambridge, Massachusetts 02142, USA*

[5]*Department of Materials Science and Chemical Engineering, Stony Brook University, Stony Brook, NY, 11794, USA*

[6]*TESCAN Tempe, LLC., Tempe, Arizona 85281, USA*

[7]*National Center for Electron Microscopy, Molecular Foundry, Lawrence Berkeley National Laboratory, Berkeley, CA 94720, USA*

[8]*Division of Chemistry, Brookhaven National Laboratory, Upton, NY, 11973, USA*

[9]*California Research Alliance (CARA), BASF Corporation, Berkeley, California 94720, USA*

Corresponding authors: mcargn@stanford.edu, sandip.de@basf.com

Abstract

Engineering colloidally stable multimetallic nanocrystals has many benefits in a wide range of applications and introduces the opportunity of manipulating physical, chemical, and electronic structure properties of materials at the nanoscale. Synthesis routes are challenged by the chemical complexity required to temporally and spatially coordinate the reduction and alloying of multiple metal species, which hampered the development of tunable libraries of colloidal materials to date. In this work, we demonstrate a synthesis method guided by machine learning-accelerated simulations to incorporate five or more metal elements in monodisperse, colloidally stable nanocrystals. Multiple seed materials can be used, leading to a library of multimetallic nanocrystals with tunable electronic, physical, and alloying structure. The advantage of this synthetic protocol is highlighted in the preparation of catalytic materials that showed two orders of magnitude higher reaction rates than monometallic catalysts and outstanding thermal stability, thus highlighting the promise of this approach for high-performance materials in many areas.

Introduction

Colloidal nanocrystals of controlled sizes, shapes, and compositions have been intensively explored for the last three decades due to their applications in various fields such as catalysis[1–5], photonics[6,7], electronics[8–12], medicine[13–15], and biomedical imaging[16–18], among others[19,20]. The precise study of well-defined nanocrystalline structures has revolutionized understanding of materials properties at the nanoscale and enabled atomic-scale engineering of materials to achieve new material properties. The physical and chemical properties of nanocrystalline materials can be tailored by changing the intrinsic size, shape, and/or composition. For these reasons, various nanocrystal systems have been developed and studied, ranging from metallic, to semiconducting, to insulating materials. Among various parameters, compositional fine-tuning of colloidal nanocrystals in multimetallic system modifies the electronic structure hybridization, thus resulting in increased controllable and tunable physical and chemical properties compared to individual metal components[21–26].

A particularly interesting example of collective properties derived from the mixing of elements is represented by high entropy alloy (HEA) materials. HEAs contain five or more metals in a single solid solution phase and show unique properties that result from the complex random atomic configuration. Metal atoms in HEAs possess varied near-neighbor arrangements, which alter their electronic structure. Therefore, atoms in HEAs could have different properties even from those present in bimetallic or trimetallic alloys[27]. In other words, HEAs expand the opportunities to engineer novel metal compositions and optimize their electronic structure for many applications. Furthermore, due to the random configuration of elements, HEAs have distorted structures with lattice strain, which results in large diffusion barriers for atoms,[28,29] which can lead to greater thermal stability.

Although many synthesis techniques for bulk or nanocrystalline forms of HEAs have been developed[25,28,30–32], there are far fewer reported colloidal syntheses. Colloidal methods are considerably attractive since they can be readily tuned to modify the composition and structure of the alloys, while also providing highly uniform materials. Developing colloidal synthesis methods is, however, challenging because of the increase in complexity in synthetic chemistry with the increase in the number of elements in the system[33]. For instance, the decomposition temperature of metal salts, the redox potential of elements, and the choice of reducing agent and ligand can affect the formation of nanocrystals[34–36]. Specifically, base metals, which are often used in bulk HEAs due to their affordability and earth abundance, have lower redox potential compared to precious metals, which leads to their challenging incorporation in colloidal multimetallic nanocrystals[37]. Furthermore, interactions between different metals further complicates the synthesis pathways, with processes such as galvanic replacement[38] and autocatalytic reduction[39], when designing colloidal synthesis pathways. Finally, homogenous nucleation of elements must be suppressed.

Due to the complexity of the synthesis, a few solution-phase synthetic methods for colloidal HEA and multimetallic nanocrystals have been reported. For instance, hot injection methods[35] and low temperature solvothermal methods[24,39] demonstrated the successful synthesis of HEA nanocrystals. However, these methods were not able to control the size and shape of the nanocrystals. Recently, seed-mediated co-reduction methods have been applied to control the size and shape of nanocrystals, where three different metals were reduced and deposited on pre-synthesized bimetallic nanocrystals, forming core-shell structures[29,40,41]. The resulting nanocrystals were then deposited on support materials and reduced at high temperature to form an HEA structure. Although various HEAs were synthesized with this method, they resulted from an additional annealing step rather than directly from colloidal preparation. In addition, these preceding methodologies have employed two or more Pt-group metals, which adds considerable cost to scaling up these syntheses.

Herein, we developed a robust method to synthesize HEA and multimetallic nanocrystals with five or more elements with only one noble metal used as a seed to grow the multimetallic, base-metal nanocrystals. We synthesized various compositions of Pt-based HEA and multimetallic nanocrystals with uniform sizes and shapes. Machine learning-based high-throughput screening methods were used to calculate the atomic scale thermodynamic phase segregation tendency in the bulk. While the modelling effort does not include any synthesis specific or reaction specific parameters for the high-throughput screening, the results provide fundamental mixing probability that we found to be successful in shortlisting potential stable compositions that could form HEA materials under our synthetic conditions. We also demonstrated the tunability and generality of the synthesis method by modifying the size and shape of seed materials, and by using other seed materials for their synthesis such as Pd and Au. Lastly, HEA nanocrystals-based catalysts showed much increased catalytic activity and thermal stability compared to bare Pt catalysts, demonstrating their potential for active, stable, and cost-effective catalysts.

Results and Discussion

The main challenge in obtaining colloidal HEA and multimetallic nanocrystals is ensuring that the decomposition/reduction of the metal precursors occurs in a predictable and controlled way to avoid homogeneous nucleation of individual metals. For this reason, attempts at starting from metal salts resulted in the uncontrolled formation of several different particles with broad size distributions and agglomeration (Figure S1). This result was certainly because of the different decomposition temperatures of metal precursors, resulting in several pathways for nucleation and growth for each element. One important discovery was that the core of the formed nanocrystals mostly contained Pt, the only noble metal used in the synthesis. Therefore, to improve the control of nanocrystal formation, a seed-mediated method using Pt seeds was developed (Figure 1a).

The computational screening described in the next section initially highlighted higher potential mixing for the combination PtFeCoNiW that we therefore chose as a first composition to

synthesize in order to showcase the approach. Uniform Pt seed nanocrystals (5.2 ± 0.7 nm, Figure 1b) were reacted with multiple base metal precursors to achieve decomposition/reduction of metal salts and alloying by metal diffusion into the Pt seeds. The resulting PtFeCoNiW nanocrystal solution was colloidally stable for many days/weeks (Figure 1c), and the nanocrystals demonstrated high uniformity in size (6.3 ± 0.8 nm, Figure 1d). The increase in size compared to the initial Pt seeds was in line with the expected amount of base metals added.

Energy-dispersive X-ray spectroscopy (EDS) maps of as-synthesized PtFeCoNiW nanocrystals demonstrated that the signal for each metal overlapped in each individual nanocrystal (Figure 1e, spectrum in Figure S2a). EDS line profiles showed that the contribution for the individual elements overlapped across each individual particle, demonstrating that each element was present across each nanocrystal in a similar concentration pattern (Figure S3). The atomic content of each element quantified using EDS was 33, 7, 19, 30, and 11% for Pt, Fe, Co, Ni, and W, respectively (Figure S2b). Multiple analyses of individual nanocrystals showed elemental distributions with less than 10% standard deviation for Pt, Fe, Co, Ni, and 15% standard deviation for W, demonstrating high compositional uniformity (Figure S4). The relatively lower content measured for Fe and W could be attributed to the presence of homogenous nucleation or galvanic replacement of elements in solution. Overall, the data suggested that colloidal nanocrystals containing all elements in approximately equal ratio were synthesized.
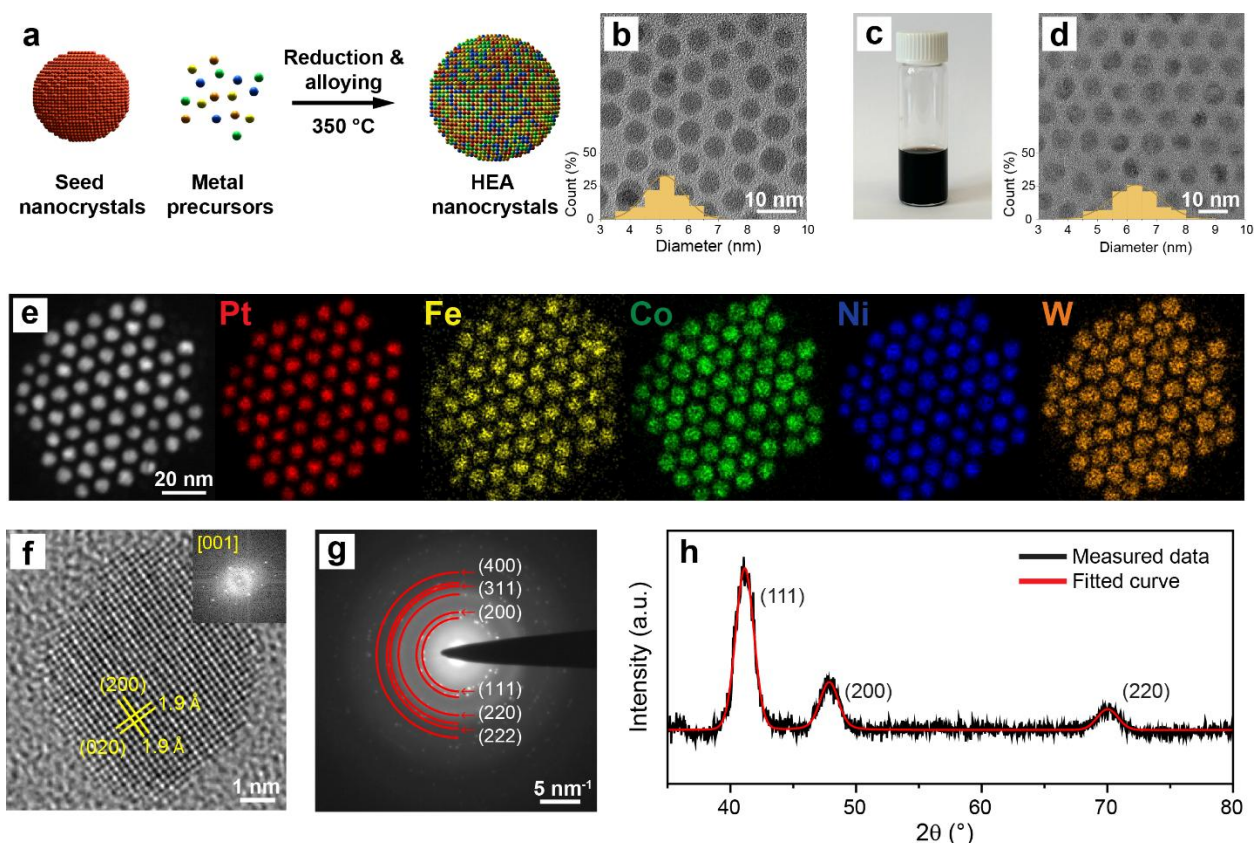
Figure 1. Seed-mediated synthesis of colloidal HEA nanocrystals. (a) Schematic of seed-mediated growth. (b) AC-HRTEM image of Pt seed nanocrystals. (c) Photograph of PtFeCoNiW nanocrystals solution. (d) AC-HRTEM image of PtFeCoNiW nanocrystals. (e) HAADF-STEM image and corresponding EDS maps of PtFeCoNiW nanocrystals. (f) AC-HRTEM image of a PtFeCoNiW nanocrystal in [001] zone axis with fast Fourier transformation image (top right). (g) SAED of PtFeCoNiW nanocrystals. (h) XRD analysis of PtFeCoNiW nanocrystals.

Aberration corrected-high resolution transmission electron microscopy (AC-HRTEM) images of a single nanocrystal were taken to investigate the crystal structure of the material (Figure 1f). The corresponding fast Fourier transformation showed the face-centered cubic (FCC) {200} lattice planes under [001] zone axis (inset in Figure 1f) with a lattice spacing of (200) measured to be 1.9 Å. Using this value, the lattice constant of a nanocrystal was calculated to be 3.8 Å, which was 3.1% smaller than that of pure Pt. We collected selected area electron diffraction (SAED) of a group of 77 nanocrystals to further confirm the presence of a single phase in the PtFeCoNiW nanocrystal sample (Figure 1g and Figure S5). The half circles in the SAED pattern indicated the reference diffraction rings of the FCC crystal structure with a lattice constant of 3.8 Å. None of the diffraction spots deviated from the diffraction rings, demonstrating the presence of a single phase in an extended number of nanocrystals. Lastly, X-ray diffraction (XRD) analysis (Figure 1h) showed three distinctive peaks (41, 48, and 70 ° 2θ) corresponding to (111), (200), and (220)

contributions from an FCC crystal structure. None of these peaks matched the XRD peaks of individual elements or their oxides (Figure S6). The lattice constant calculated based on XRD peaks was 3.8 Å, in line with what was found by AC-HRTEM and SAED. These results demonstrated that microscopic and bulk characterization of the nanocrystal structure matched. In summary, they confirmed the formation of a solid solution of five metal elements in colloidally stable nanocrystals.

Motivated by the successful development of a synthesis method to produce colloidal HEA nanocrystals, we expanded the potential compositional space by screening other Pt-containing compositions using machine learning (ML)-based simulations. A high-throughput screening method was used to predict the phase mixing and segregation in nanocrystals and identify optimal compositions for HEA formation from Pt and eleven transition metals (Ag, Co, Cr, Cu, Fe, Mn, Mo, Ni, V, W, Zn), chosen for their reduction potential and technological interest in the final material compositions. Atomic structures containing equimolar amounts of five elements in FCC structures were generated with random orderings, followed by high-throughput replica-exchange molecular dynamics and Monte Carlo atom swaps (REMD/MC) simulations for all bulk compositions. We analyzed the last 3000 steps of the low-temperature replica at 500 K for each HEA composition from its REMD/MC trajectory. The segregation propensity of each atom pair was then characterized by the average Cowley's short-range order (SRO) parameters[42]. Specifically, a near-zero SRO value indicated a well-mixed system with randomly distributed atoms. Increasingly negative SRO values suggested a stronger preference for specific atom pairs to aggregate. Conversely, values approaching 1 implied a lower probability of those atom pairs existing as nearest neighbors. Minimum average SRO corresponded to the atom pair that was lowest in average SRO value over the REMD/MC trajectory, while the average SRO standard deviation characterized the variation in average SRO values among all atom pairs. Thus, a higher minimum average SRO and lower average SRO standard deviation implied a higher probability of phase mixing. The full high-throughput screening results can be found in Table S1.

The calculated minimum average SRO and average SRO standard deviation of various compositions were plotted (Figure 2a), and the SRO correlation of metals from the calculated SRO of various compositions was summarized (Figure 2b). In addition to the promising PtFeCoNiW (low SRO) composition that was discussed in the previous section, five compositions that had relatively low (PtVFeNiMo), medium (PtCrNiCuZn, PtMnFeCoNi), and high (PtCoNiCuZn) minimum average SRO were synthesized as well to test the predictive capabilities of the simulation (Figure S7 reports SRO values for the highlighted compositions).

In the PtFeCoNiW composition, the atomic structure constructed by simulation showed a random distribution of elements (Figure 2c). All atomic pairs showed a minimum average SRO value above -0.67 and an average standard deviation of 0.44 across all temperatures (Figure 2d). As expected from the simulation, the PtFeCoNiW nanocrystals demonstrated a homogenous distribution and mixing of all five elements, demonstrating HEA formation (Figure 1).
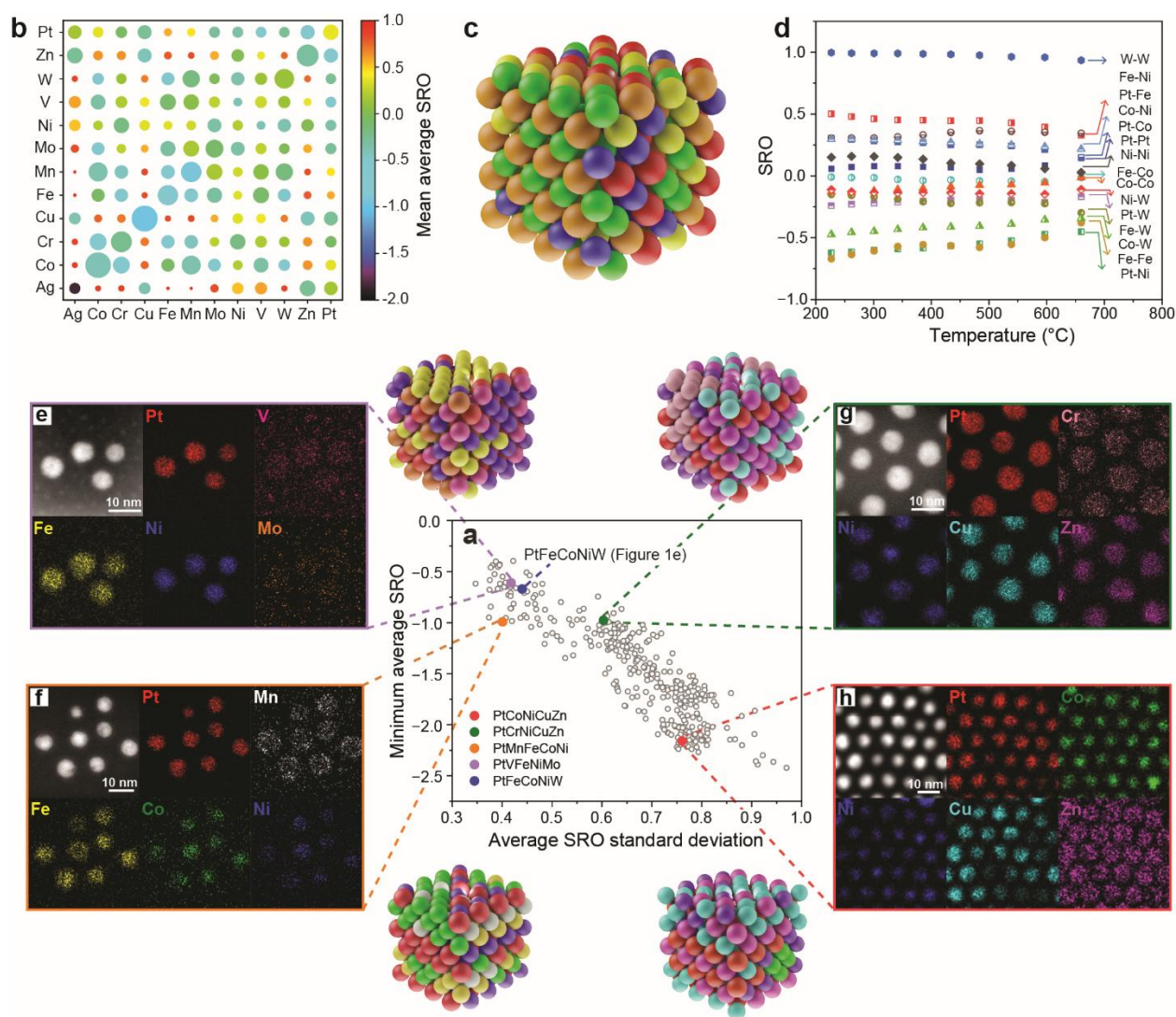
Figure 2. Machine learning-based high-throughput screening of metal compositions. (a) Scatter plot of the minimum average SRO versus the standard deviation of average SRO. (b) correlation plot of the mean (indicated by circle color) and standard deviation (indicated by circle radius) of the average SRO (from the last 3000 REMD/MC steps) for atom pairs in equimolar Pt-based bulk HEAs with four other elements chosen from 11 transition metals. (c) Atomic structure model of PtFeCoNiW (Red: Pt, yellow: Fe, green: Co, blue: Ni, and orange: W) (d) SRO of all possible atomic pairs in PtFeCoNiW at different temperatures. (e-h) HAADF-STEM image, EDS maps, and atomic structure models of various nanocrystals; (e) PtVFeNiMo, (f) PtMnFeCoNi, (g) PtCrNiCuZn, and (h) PtCoNiCuZn. Corresponding EDS spectra are presented in Figure S8.

The PtVFeNiMo composition, which had a comparable average SRO to PtFeNiCoW, was then synthesized. Although it was a promising composition found from the simulations, only Pt, Fe,

and Ni were majorly present in the final nanocrystals, while V and Mo were present in much lower atomic percentages and formed individual clusters or particles (Figure 2e and FigureS8a). Other compositions that included either Mo or V or both in the precursors (PtCoNiMoW, PtFeCoNiMo, and PtVCrMnFe) did not result in appreciable amounts of these elements in the final nanocrystal products (Figure S9). The reason could be the intrinsic difficulty in reducing the ion to the metallic state, thus leading to precipitation of oxide phases or homogeneous nucleation in solution.

Then, the PtMnFeCoNi composition with a similar average minimum SRO and average SRO standard deviation to PtVFeNiMo was synthesized. In this case, all five elements were present in the nanocrystals and were well mixed, with Mn being mostly concentrated in the outer portion of each nanocrystal (Figure 2f). We hypothesized that a galvanic reaction between other metals and Mn resulted in the formation of the Mn shell since it has the lowest redox potential, or it is possible that Mn oxidized when exposed to air after synthesis. Nevertheless, it demonstrated that the synthesis was successful when metals that were more easily reducible than V and Mo were used.

A similar trend was observed in the PtCrNiCuZn composition, which had a similar minimum average SRO compared to PtMnFeCoNi but with higher average SRO standard deviation. In this case, Cr was also concentrated in the outer portion of each nanocrystal with a relatively lower atomic ratio (6.3%, Figure 2g, and Figure S8c). This composition also formed multimetallic nanocrystals with the five elements present in compositional uniformity across the entire nanocrystal population, in agreement with simulations.

Finally, the simulation results suggested that replacing Cr with Co to prepare PtCoNiCuZn could result in phase segregation given the lower relative minimum average SRO (Figure 2a). The nanocrystal products for this composition showed the presence of all five elements in each nanocrystal (Figure 2h), but domains with high Cu and low Co and Ni concentrations were present, indicating that metals segregated after deposition (Figure S10). As shown in the SRO correlation plot (Figure 2b), the simulations also confirm that Cu-containing HEA compositions are generally more likely to have strong segregation. Furthermore, the simulation showed that Co had the strongest segregation tendency in the PtCoNiCuZn composition with a minimum average SRO of -2.16 (Figure S7d). Nevertheless, all five elements were present in each nanocrystal, leading to colloidally stable multimetallic particles. Overall, the synthesis results confirmed the trends described by the simulations, leading to a good agreement and to the opportunity of preparing a variety of multimetallic nanocrystals following the SRO values derived by simulation.

The seed-mediated approach could be advantageously used to finely tune many structural parameters including size and composition by manipulating the seed material. Size control was demonstrated by using Pt nanocrystal seeds with a smaller average diameter of 2.2 ± 0.3 nm (Figures 3a-b). The obtained PtFeCoNiW nanocrystals grew to a 2.6 ± 0.3 nm average diameter (Figures 3b-c), and EDS maps demonstrated the homogenous distribution of five elements across each individual nanocrystal (Figures 3d).

Extension of the seed material composition was demonstrated by using Au and Pd seeds in place of Pt seeds. Au nanocrystals with an average diameter of 4.6 ± 0.4 nm were synthesized (Figures

3e-f) and used to prepare AuCoNiCuZn nanocrystals. The resulting nanocrystals showed an average diameter of 6.7 ± 1.1 nm (Figures 3f-g). In the HAADF-STEM image, a variation in contrast was observed among different nanocrystals (Figure 3h), indicating the presence of multiple phases and the segregation of certain elements. Nevertheless, it was confirmed by EDS maps that all five elements were present in each nanocrystal (Figure 3h). Additionally, Pd nanocrystals with an average diameter of 7.9 ± 0.7 nm were used as seeds (Figures 3i-j) to prepare PdCoNiCuZn nanocrystals. The particle size of the produced nanocrystals increased to 12.4 ± 1.5 nm (Figures 3j-k). A similar phase segregation was observed in HAADF-STEM images and EDS maps (Figure 3l). In this case, it was more apparent that Pd, Cu, and Zn formed a single phase with higher contrast, indicating their mixing, whereas Co and Ni segregated into a phase with lower contrast, indicating their preference for mixing compared to the other metals. Again, all five elements were incorporated into each individual nanocrystal.
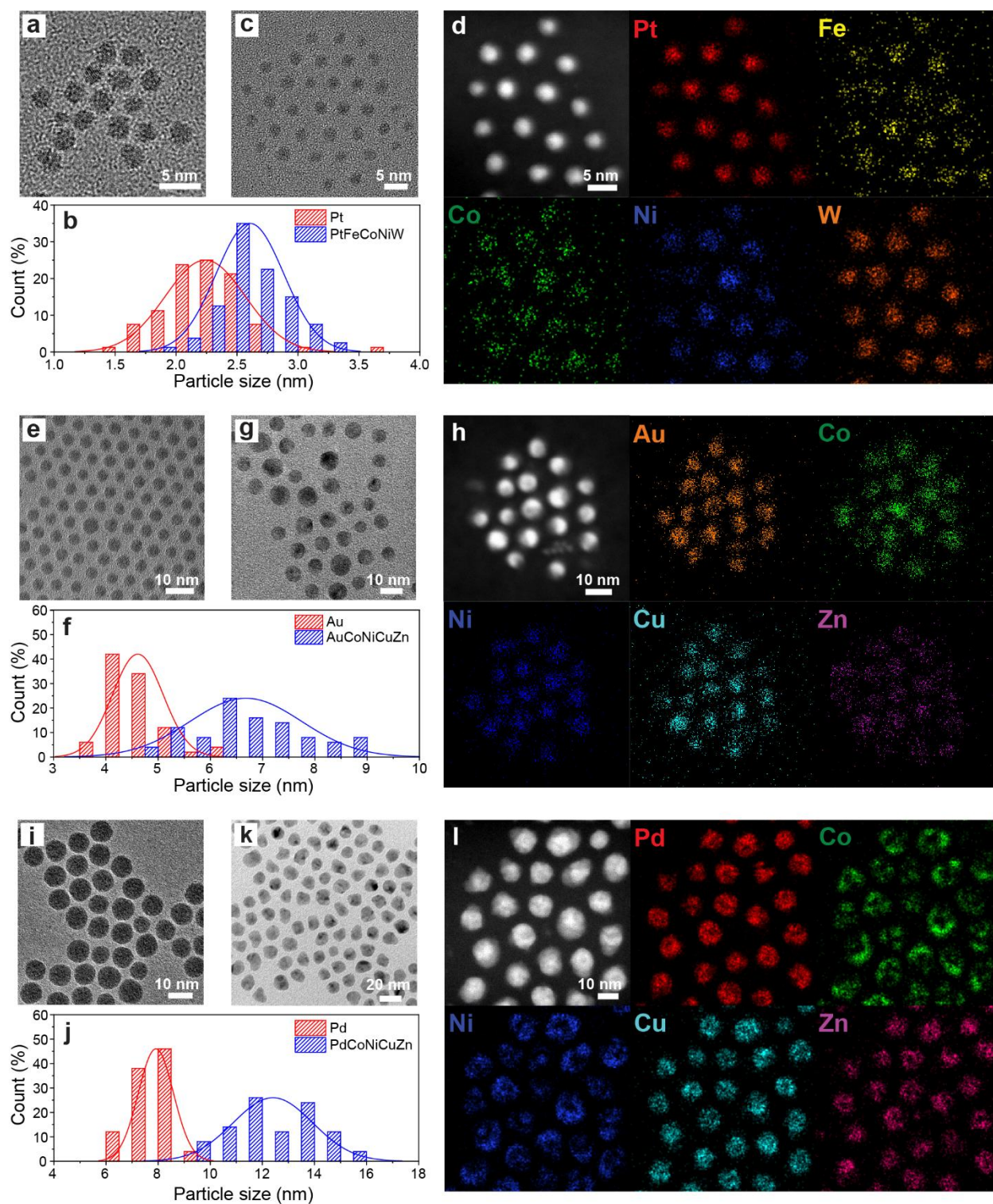
Figure 3. Versatility of seed-mediated growth method. (a) BF-TEM image of 2.2 nm Pt nanocrystals. (b) Particle size distribution of Pt and PtFeCoNiW nanocrystals. (c) BF-TEM image of PtFeCoNiW nanocrystals. (d) HAADF-STEM image and corresponding EDS maps of PtFeCoNiW nanocrystals. (e) BF-TEM image of Au nanocrystals. (f) Particle size distribution of

Au and AuCoNiCuZn nanocrystals. (g) BF-TEM image of AuCoNiCuZn nanocrystals. (h) HAADF-STEM image and corresponding EDS maps of AuCoNiCuZn nanocrystals. (i) BF-TEM image of Pd nanocrystals. (j) Particle size distribution of Pd and PdCoNiCuZn nanocrystals. (k) BF-TEM image of PdCoNiCuZn nanocrystals. (l) HAADF-STEM image and corresponding EDS maps of PdCoNiCuZn nanocrystals. Corresponding EDS spectra are in Figure S11.

The mechanism of formation of mixed phases in the final multimetallic nanocrystals was studied by varying the size and shape of the used seed Pt nanocrystals. PtCoNiCuZn composition was used as a model composition to track the degree of mixing. Many factors, such as the morphology or composition of seed nanocrystals, can affect the diffusion and mixing of metals in the seed-mediated growth process. The ratio of undercoordinated sites (terrace, edge, and corner) is size-dependent and can change the reactivity of surface atoms[43]. The type of exposed facets is shape-dependent, which could alter the energy barrier for metal deposition and diffusion of atoms[43,44].

PtCoNiCuZn nanocrystals obtained from smaller Pt seeds (3.9 ± 0.3 nm, Figure 4a and Figure S12a) demonstrated uniform sizes (5.1 ± 0.6 nm, Figure 4b and Figure S13a) and a homogenous distribution of the five elements (the light-contrast shell in the HAADF-STEM image was formed during EDS collection, Figure S14). Pt nanocrystals with faceted surfaces were synthesized (6.8 ± 0.5 nm, Figure 4c and Figure S12b) and the prepared PtCoNiCuZn nanocrystals showed a rather uniform size of 10.7 ± 1.2 nm but with a clear core-shell structure (Figure 4d and Figure S13b). Pt, Cu, and Zn resided in the core, and Co and Ni were present in the shell. Finally, Pt cubes (10.3 ± 1.0 nm), whose surfaces were mainly enclosed by {100} facets (Figure 4e and Figure S12c), produced PtCoNiCuZn nanocrystals with very heterogeneous structures and a clear bright core and a diffused shell. The core was 9.4 ± 1.4 nm in size, while the entire particles were 19.8 ± 2.5 nm in size (Figure S13c). EDS revealed that the core portion was essentially composed of only Pt, while the shell was a mixture of the base metals deposited on the Pt cubes facets, indicating no significant diffusion or mixing of the elements with Pt (Figure 4f). Overall, the results reveal a clear size- and shape-dependency in the mixing of elements in the final multimetallic nanocrystals.
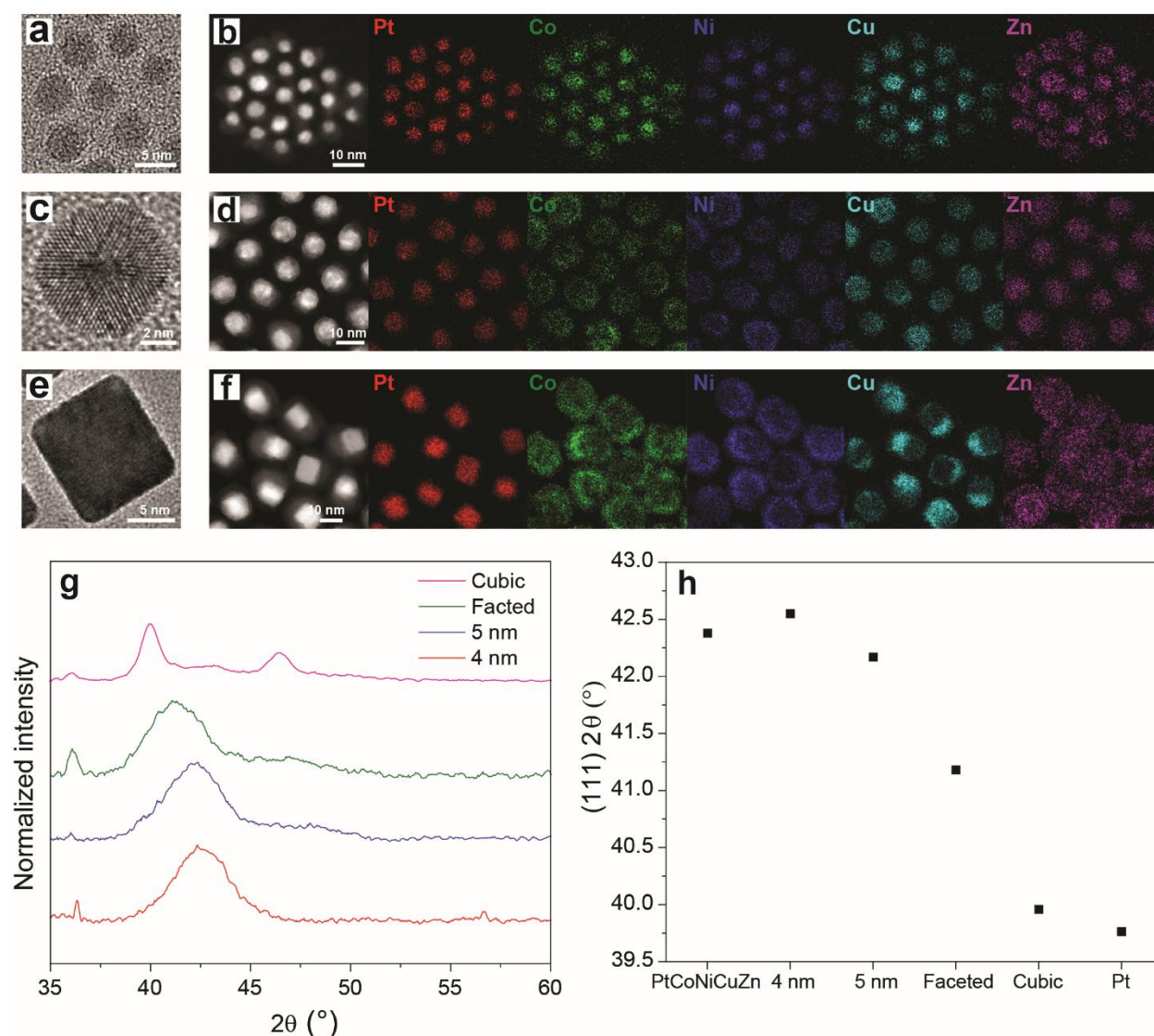
Figure 4. The effect of size and shape of seed nanocrystals on the degree of alloying of multimetallic nanocrystals. (a) BF-TEM image of 3.9 nm Pt seed nanocrystals. (b) HAADF-STEM image and corresponding EDS maps of PtCoNiCuZn nanocrystals grown from smaller seeds. (c) BF-TEM image of faceted Pt seed nanocrystals. (d) HAADF-STEM image and corresponding EDS maps of PtCoNiCuZn nanocrystals grown from faceted seeds. (e) BF-TEM image of Pt cube nanocrystals. (f) HAADF-STEM image and corresponding EDS maps of PtCoNiCuZn nanocrystals grown from cubic-shaped seeds. (g) XRD spectra of various sizes and shapes of PtCoNiCuZn nanocrystals. (h) (111) 2θ of Pt and PtCoNiCuZn references and the different sizes and shapes of synthesized PtCoNiCuZn nanocrystals. Corresponding EDS spectra are in Figure S15.

XRD patterns of all the nanocrystal products were collected to understand the changes in the degree of mixing using the different seeds (Figure 4g). The (111) 2θ peak of PtCoNiCuZn grown

from small seeds was 42.5 °, a higher value compared to that of nanocrystals produced from 5 nm seeds (42.1 °) and in line with the value (42.4 °) that was calculated from Vegard's law for this composition (Table S2)[45]. In combination with the EDS characterization (Figure 4b), this result indicated a high degree of mixing of metals in smaller nanocrystals to form the HEA, which agreed with previous studies[46]. HEA formation was likely aided by diffusion of metals through shorter distances and undercoordinated sites on the seed surface. A decrease in nanoparticle size could decrease the Gibbs free energy to obtain the HEA due to the change in cohesive energy and could result in the mixing of immiscible elements at the nanoscale[46,47].

The (111) 2θ peak of the nanocrystals prepared from faceted seeds was found at 41.2 ° (Figure 4g), implying a lower degree of alloying that aligned with what was observed from EDS maps (Figure 4d). Previous studies demonstrated that corner, edge, and face sites have different energy barriers for the deposition of metals, and that terrace sites on large facets have the highest energy barrier for deposition[43]. It is also known that defect sites, such as twin defects present in the faceted Pt seeds, could lead to autocatalytic reduction with lower activation energy than other sites to accelerate the deposition of metals[44]. Based on this knowledge, we hypothesized that Cu and Zn were selectively deposited on edges sites, followed by Co and Ni deposition.

The (111) 2θ peak of the nanocrystals prepared from cubic seeds was close to the Pt reference peak (Figure 4g), indicating very minimal, if any, alloying. The minute peak shift could be due to a small degree of alloying or lattice strain effects from the core-shell structure[48–50]. EDS suggested the preferred deposition of copper on the Pt seeds over other metals, which was different from the structure of spherical Pt nanocrystals. It is possible that the Pt(100) facet selectively catalyzed the reduction of the copper precursor, followed by the deposition of other elements on the copper phase. In addition, asymmetric growth of Cu was observed, which could have been due to the lattice mismatch causing a slow deposition rate or surface diffusion[51–53]. Very limited diffusion of other metals into the Pt lattice was observed, indicating that the diffusion barrier on the ordered (100) surface was higher than that for the disordered spherical Pt surface, rich in defect sites[54,55].

The (111) 2θ peak positions for all the PtCoNiCuZn nanocrystals were summarized in Figure 4h. These results demonstrate that selection of seed size and shape has a large influence on the final alloying and deposition of alloyed metals. Therefore, this method allows to obtain a variety of colloidal nanocrystal products ranging from HEA to multimetallic colloidal nanocrystals with control over alloying degree and structure. This result is challenging to achieve with other synthesis methods.

HEAs are often considered promising materials for catalytic applications because of their structural stability and catalytic activity, which originates from their unique lattice and electronic structures[56–58]. A unique advantage of colloidal HEA nanocrystals prepared in this work is that they can be deposited onto any support for catalysis, thus allowing to finely engineer metal-support interactions and obtain active and stable catalysts. In this case, alumina-supported PtFeCoNiW nanocrystals were investigated for their catalytic performance and stability by comparing them to

Pt-only catalysts. Both PtFeCoNiW and Pt nanocrystals were deposited on commercial γ-Al_2O_3, and residual organic ligands were removed by thermal treatment after deposition[59]. The catalysts had similar average nanoparticle sizes after thermal treatment (4.8 ± 1.6 nm for Pt/Al_2O_3 and 6.4 ± 1.0 nm for PtFeCoNiW/Al_2O_3, Figure 5a and Figure S16a-b). To test their thermal stability, catalysts were aged under hydrothermal conditions in oxygen and steam at 600 °C and 650 °C for 6 hours, a condition that is largely used in emission control applications. Pt/Al_2O_3 significantly sintered after aging, with a final average particle size that increased to 12.8 ± 7.1 nm and 18.3 ± 11 nm, respectively, and a very broad particle size distribution indicative of vapor-phase sintering via volatile PtO_x species (Figure 5a and Figure S16d and f)[60–62]. In contrast to Pt/Al_2O_3, PtFeCoNiW/Al_2O_3 catalysts maintained their size after aging at 6.7 ± 0.9 nm and 6.8 ± 3.3 nm, respectively, with only marginal changes to their size distribution likely due to agglomeration of particles in very close distance (Figure 5a and Figure S16c and e). The thermal stability of the HEA catalyst was remarkable considering the tendency of Pt-based catalyst to sinter under hydrothermal conditions[63–65].
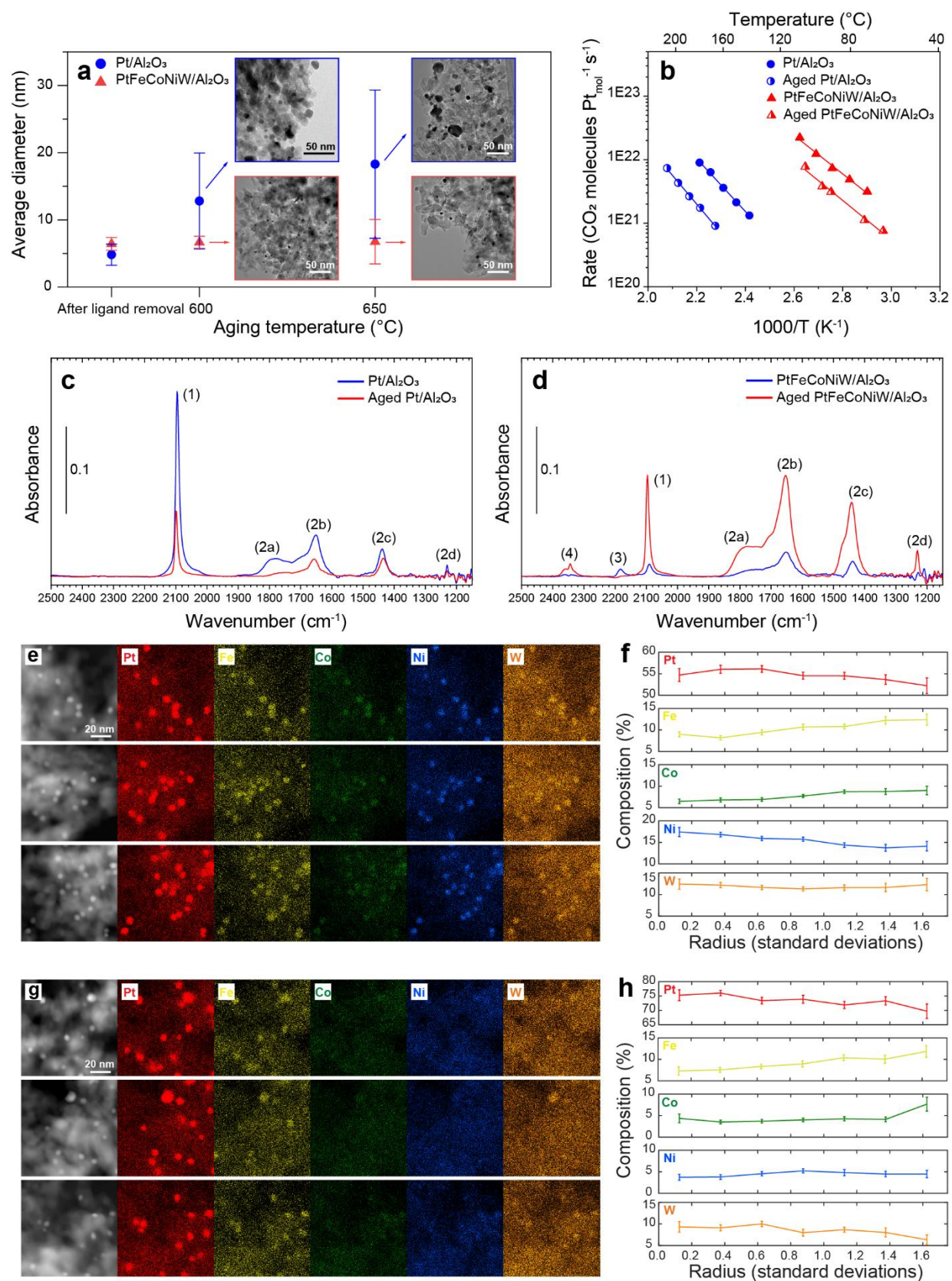
Figure 5. The stability and activity of PtFeCoNiW/Al$_2$O$_3$ catalysts. (a) Average diameter plots of Pt/Al$_2$O$_3$ and PtFeCoNiW/Al$_2$O$_3$ after aging at different temperatures with BF-TEM images of aged catalysts. (b) CO oxidation steady-state rate of Pt/Al$_2$O$_3$ and PtFeCoNiW/Al$_2$O$_3$ before and after 650 °C 6 hours hydrothermal aging. (c) CO-DRIFTS spectra of Pt/Al$_2$O$_3$ before and after 650 °C 6 hours hydrothermal aging with gas phase CO signal subtraction. (d) CO-DRIFTS spectra of PtFeCoNiW/Al$_2$O$_3$ before and after 650 °C 6 hours hydrothermal aging with gas phase CO signal subtraction. (e) HAADF-STEM image and corresponding EDS maps of PtFeCoNiW/Al$_2$O$_3$ after ligand removal. (f) Elemental compositions versus nanoparticles radius plots of Pt, Fe, Co, Ni, and W. The data was extracted from EDS maps in Figure 5e. (g) HAADF-STEM image and corresponding EDS maps of PtFeCoNiW/Al$_2$O$_3$ after 650 °C 6 hours hydrothermal aging. (h) Elemental compositions versus nanoparticles radius plots of Pt, Fe, Co, Ni, and W. The data was extracted from EDS maps in Figure 5g.

The catalytic activity of PtFeCoNiW/Al$_2$O$_3$ catalysts was tested using CO oxidation as a probe reaction, because Pt is well known to be an active metal.[66–68] The PtFeCoNiW/Al$_2$O$_3$ catalyst reached the same rate at a lower temperature than Pt catalysts, showing its higher catalytic activity (Figure 5b). To quantitatively compare the activity of two catalysts at the same temperature, the rate of PtFeCoNiW/Al$_2$O$_3$ catalyst was quantified and compared. The PtFeCoNiW/Al$_2$O$_3$ catalyst showed 40 times higher rate (3.6×10^{23} CO$_2$ molecules Pt$_{mol}^{-1}$ s^{-1}) than Pt/Al$_2$O$_3$ catalyst (9.0×10^{21} CO$_2$ molecules Pt$_{mol}^{-1}$ s^{-1}) at 180 °C. Furthermore, the activity difference became more significant after aging the two catalysts at 650 °C for 6 hours. The rate of aged PtFeCoNiW/Al$_2$O$_3$ catalyst at 180 °C (1.6×10^{23} CO$_2$ molecules Pt$_{mol}^{-1}$ s^{-1}) was about 100 times higher compared to Pt/Al$_2$O$_3$ catalyst (1.7×10^{21} CO$_2$ molecules Pt$_{mol}^{-1}$ s^{-1}).

To understand the origin of the high activity of PtFeCoNiW/Al$_2$O$_3$ catalysts, we characterized the surface of the supported nanoparticles using CO chemisorption and CO diffuse reflectance infrared Fourier transform spectroscopy (CO DRIFTS). In the chemisorption experiments, PtFeCoNiW/Al$_2$O$_3$ catalysts demonstrated a CO uptake of 1.41 µmol g^{-1} compared to 2.54 µmol g^{-1} for monometallic Pt catalysts (Table S3 and Figure S17a-b). This data indicated that PtFeCoNiW/Al$_2$O$_3$ catalysts had fewer active sites for binding CO than Pt/Al$_2$O$_3$ catalysts, likely due to less Pt atoms on the surface than Pt/Al$_2$O$_3$ catalysts. CO-DRIFTS was used to investigate the active surface. Pt/Al$_2$O$_3$ catalysts showed an intense peak around 2105 cm^{-1}, which we attribute to linearly bound CO on well-coordinated Pt sites[69], consistent with previous measurements over Pt (111) single crystals[70] and Pt nanoparticles[71] (Figure 5c and Table S4, baseline-corrected CO-DRIFTS spectra with gas phase CO are included in Figure S18). We also observed multiple peaks related to carbonates on Al$_2$O$_3$ (1800, 1655, 1440, and 1230 cm^{-1}).[72] Multi-bound CO on Pt surfaces[73] would also appear at approximately 1800 cm^{-1}, but it was difficult to deconvolute the peak from the Al$_2$O$_3$-related carbonate peak (Figure 5c). In contrast, PtFeCoNiW/Al$_2$O$_3$ had a relatively weak peak around 2105 cm^{-1}, which supports the hypothesis that there was less Pt on the PtFeCoNiW/Al$_2$O$_3$ surface compared to Pt/Al$_2$O$_3$ catalysts (Figure 5d). While DRIFTS is

difficult to perform quantitatively, given the similar mass and weight loading of the catalysts, qualitative comparisons are still valid. The PtFeCoNiW/Al$_2$O$_3$ catalysts also showed a peak around 2180 cm^{-1} that was not present in Pt/Al$_2$O$_3$ catalysts (Figure 5d). This peak aligned well with frequencies expected for CO adsorbed on Fe[74], Co[75], Ni[76], and Pt[77] oxide sites; as such, it was not possible to assign a given site directly using DRIFTS. Thus, we conclude that metal oxides were present on the surface of PtFeCoNiW/Al$_2$O$_3$ catalysts and that they covered the Pt sites.

We used X-ray absorption spectroscopy (XAS) to further investigate the structure of PtFeCoNiW/Al$_2$O$_3$ catalysts. Due to the similarity between photoelectron scattering amplitudes of Fe, Co, and Ni nearest neighbors to Pt, their contributions to Pt L$_2$-edge extended X-ray absorption fine structure (EXAFS) could not be separated and were represented by an effective Pt-metal scattering path. For W, due to its proximity to Pt in the periodic table and smaller fraction compared to Pt in the alloy, its contribution was not distinguishable from Pt neighbors, and the effective Pt-Pt path accounted for both Pt and W contributions. EXAFS data analysis revealed that the coordination number of Pt-Pt and Pt-metal nearest neighbor bonds were 7.9 ± 2.1 and 4.2 ± 1.8, respectively (Table S5, S6 and Figure S19). In addition, all metals except Pt were mostly present in their oxide form (Figure S20-22).

Two structural models could be proposed from XAS and surface characterization data. One was a model featuring a small Pt core with a metal oxide shell; another was a Pt-rich HEA core and a metal oxide shell. EDS maps of PtFeCoNiW/Al$_2$O$_3$ catalysts were taken to confirm our models. Data fitting was done in EDS maps to improve the signal-to-noise and obtain elemental distribution with high resolution (details in the method section). All five elements were present across the nanoparticles in EDS maps (Figure 5e). Compositional quantification showed that the Pt atomic ratio was ~55 %, and that of Fe, Co, Ni, and W were ~10, ~8, ~15, and ~12%, respectively, in the core of the particle. In addition, we found that the atomic ratio of Pt decreased from core to shell while the atomic ratio of Co and Fe gradually increased (Figure 5g). This data indicated that nanoparticles had a Pt-rich HEA core and base metal-rich shell structures that matched our second proposed model. This result also agreed with previous reports, where PtFeCoNiCu HEA nanoparticles were converted into Pt-rich HEA core and oxide shell structures after exposure to oxidative conditions.[78] The oxidation of PtFeCoNiW possibly occurred during particle washing or when it was exposed to air during the ligand removal process.

Based on its core-shell structure, we hypothesize that the high activity of PtFeCoNiW/Al$_2$O$_3$ catalysts came from the contribution of surface metal oxides. The interface between Pt and reducible metal oxides, such as Co$_3$O$_4$ and NiO, are active sites for CO oxidation[79–81].The apparent activation energy difference between Pt/Al$_2$O$_3$ (80 kJ mol^{-1}) and PtFeCoNiW/Al$_2$O$_3$ (58 kJ mol^{-1}) catalysts supported this hypothesis. The activation energy for Pt/Al$_2$O$_3$ was similar to previously reported values, and the activation energy for PtFeCoNiW/Al$_2$O$_3$ catalysts was closer to the value of Pt supported on reducible oxides,[82,83] where active sites are the interface between Pt and metal oxides.

CO-chemisorption and CO-DRIFTS were performed on the 650 °C aged PtFeCoNiW/Al$_2$O$_3$ and Pt/Al$_2$O$_3$ catalysts to investigate surface structure changes. The CO uptake increased after aging for the PtFeCoNiW/Al$_2$O$_3$ catalyst (2.05 µmol g^{-1}), while the CO uptake of the Pt/Al$_2$O$_3$ catalyst significantly decreased (0.99 µmol g^{-1}) (Table S3 and Figure S17c-d). The results agreed with TEM size distribution analysis indicating sintering (Figure 5a and Figure S16e-f). In CO-DRIFTS, the PtFeCoNiW/Al$_2$O$_3$ catalysts showed an intense linear CO peak (2105 cm^{-1}), indicating more available Pt sites compared to the catalyst before aging (Figure 5d). In contrast, the intensity of the peak around 2105 cm^{-1} decreased in the Pt/Al$_2$O$_3$ catalyst after aging, indicating loss of surface Pt atoms (Figure 5c). Interestingly, the aged PtFeCoNiW/Al$_2$O$_3$ catalyst showed a significantly increased amount of carbonate peaks (1800, 1655, 1440, and 1230 cm^{-1}) compared to the fresh PtFeCoNiW/Al$_2$O$_3$ catalyst, which could indicate some change in the metal/support interaction.

The nanoparticle composition was quantified using EDS maps after aging. Signals of all five elements were detected in each individual nanoparticle (Figure 5g). The Pt atomic ratio reached ~73% in the core, and the ratio of other base metals decreased after aging (Figure 5h). The data suggested compositional restructuring occurring during aging. Nevertheless, all five elements were still present in the core and shell components. The very few sintered particles after aging consisted of ~90% Pt (Figure S23). We therefore hypothesize that the removal of a small fraction of the base metal components was the driving force for maintaining the particle size distribution and for exposing and stabilizing platinum, akin to distillation processes described by other researchers[84].

Conclusions

A seed-mediated growth method to synthesize colloidally stable HEA and multimetallic nanocrystals was developed. Machine learning-based high throughput screening suggested the compositional space to form HEA and directed the synthesis efforts. Various compositions of multimetallic and HEA nanocrystals with five elements were synthesized by changing the size, shape, and nature of the metal seeds. Finally, PtFeCoNiW/Al$_2$O$_3$ showed higher thermal stability and catalytic activity compared to Pt/Al$_2$O$_3$ due to the presence of base metal oxides around the high entropy multimetallic core. After 650 °C hydrothermal aging, PtFeCoNiW/Al$_2$O$_3$ showed a 100 times higher Pt mass-based rate than Pt/Al$_2$O$_3$. This work demonstrates a versatile colloidal route to synth HEA and multimetallic nanocrystals with potential applications in catalysis and many areas of materials chemistry.

Methods

Synthesis of various Pt nanocrystal seeds

All nanocrystals were synthesized using colloidal synthesis with standard Schlenk line techniques.

For 2 nm Pt nanocrystals synthesis, 10 mL of trioctylamine (TOA, 98%, Sigma Aldrich), 0.66 mL of 1-oleylamine (OLAM, 98%, Sigma Aldrich), and 2.5 mL of oleic acid (OLAC, 90%, Sigma Aldrich) were added to 78.8 mg of platinum (II) acetylacetonate ($Pt(acac)_2$, 99.98%, Sigma Aldrich) in a 25 mL three-neck flask. The solution was degassed ($<$ 2 Torr) for 15 min at room temperature with stirring of a magnetic stir-bar. Then, 60 µL of trioctylphosphine (TOP, 97 %, Sigma Aldrich) was added to the flask, and the flask was heated to 120 °C using a heating mantle. The solution was further degassed for 30 minutes at 120 °C. The flask was then backfilled with nitrogen and maintained under a nitrogen atmosphere for the remainder of the synthesis. The flask was heated to 300 °C at a rate of ~20 °C min^{-1} and kept at this temperature for 30 min. The flask was cooled under blowing air to 160 °C and then placed in a water bath to cool to room temperature. The nanocrystals were isolated by precipitation with the addition of isopropanol and ethanol and then centrifugation (838 rad s^{-1}, 3 minutes). They were then redissolved in 5 mL of hexane. This procedure was repeated two times, and nanocrystals were finally redissolved in hexane for further use.

For 4 nm and 5 nm nanocrystals, 440 µL and 220 µL of TOP were used, respectively, and the final synthesis temperature was 350 °C. The remainder of the procedure was the same as for the 2 nm Pt nanocrystal synthesis described above.

Faceted Pt nanocrystals were synthesized using the previously reported methods with minor modifications[85]. 100 mg of $Pt(acac)_2$, 14 mL of OLAM, and 4 mL of 1-octadecene (ODE, 90%, Acros Organics) were mixed in a 50 mL three-neck flask with a magnetic stir bar. The solution was degassed ($<$ 2 Torr) for 1 hour at 90 °Cwith stirring of a magnetic stir-bar. Then, the flask was backfilled with nitrogen, and 1 mL of formaldehyde (ACS reagent, 37 wt. % in H_2O, Sigma Aldrich) was injected. The flask was heated to 180 °C with a ramping rate of 3 °C min^{-1} and stayed at that temperature for 2 hours. After 2 hours, the flask was cooled down to room temperature. The nanocrystals were isolated by precipitation with the addition of isopropanol and then centrifugation (838 rad s^{-1}, 3 minutes). They were then redissolved in 5 mL of hexane. This procedure was repeated two times, and nanocrystals were kept in hexane.

Cubic-shaped Pt nanocrystals were synthesized using a previously reported method with minor modifications[86]. 80 mg of $Pt(acac)_2$, 33 mL of OLAM, and 8 mL of OLAC were mixed in a 150 mL three-neck flask with a magnetic stir bar. The solution was degassed ($<$ 2 Torr) for 30 minutes at 130 °C with stirring. In a separate scintillation vial, 200 mg of tungsten hexacarbonyl ($W(CO)_6$, 97%, Sigma Aldrich) was dissolved in 8 mL of OLAM at 70 °C. The $W(CO)_6$ solution was injected into the $Pt(acac)_2$ solution. Then, the temperature was raised to 240 °C and kept for 30 minutes with stirring. The flask was cooled down to room temperature and nanocrystals were isolated by

precipitation with the addition of isopropanol and then centrifugation (838 rad s^{-1}, 3 minutes). They were then redissolved in 5 mL of hexane. This procedure was repeated, and nanocrystals were kept in hexane.

Synthesis of Au and Pd nanocrystal seeds

Au nanocrystals were synthesized using a reported procedure with few modifications[87,88]. 200 mg of gold(III) chloride trihydrate (HAuCl$_4$·3H$_2$O, ACS Reagent grade, Acros Organics) was dissolved in a stirring solution containing 20 mL of OLAM and 20 mL of 1,2,3,4-tetrahydronaphthalene (tetralin, 98%, Acros Organics) under a nitrogen atmosphere. In a separate scintillation vial, 90 mg of the borane tert-butylamine complex (TBAB, 97%, Sigma Aldrich) was dissolved in 2 mL of OLAM and 2 mL of tetralin using sonication. Then, the TBAB solution was quickly injected into HAuCl$_4$ solution at room temperature. The solution was stirred at room temperature for 1 hour after injection. The nanocrystals were isolated by precipitation with the addition of isopropanol and ethanol and then centrifugation (838 rad s^{-1}, 3 minutes). They were then redissolved in 5 mL of hexane. This procedure was repeated again, and nanocrystals were kept in hexane.

Pd nanocrystals were synthesized following a reported method[89]. 304.6 mg of palladium(II) acetylacetonate (Pd(acac)$_2$, 99%, Sigma Aldrich), 40 mL of ODE, 0.95 mL of OLAC, and 3.3 mL of OLAM were mixed in a 150 mL three-neck flask with a magnetic stir bar. The flask was degassed (< 2 Torr) for 15 minutes at room temperature with stirring. Then, 1.7 mL of TOP was added to the flask, and the flask was heated to 50 °C for 30 minutes. The reaction flask was then flushed with nitrogen and rapidly heated (~40 °C min^{-1}) to 290 °C. After 15 minutes, the flask was cooled down to room temperature. The nanocrystals were isolated by precipitation with the addition of isopropanol and then centrifugation (838 rad s^{-1}, 3 minutes). They were then redissolved in 5 mL of hexane. This procedure was repeated two times, and nanocrystals were kept in hexane.

Synthesis of colloidal HEA and multimetallic nanocrystals

First, the concentration of seed nanocrystal solution was measured by thermogravimetric analysis (TGA). 200 μL of nanocrystal solution was added dropwise into a pre-weighted aluminum TGA pan, which was heated on a hot plate at ~100 °C. This pan was then heated at 500 °C for 30 minutes in the furnace to remove all organics. Then, the final weight (pan and metal or metal oxide) was measured to calculate the concentration. 0.1 mmol of seed metal was added into the 25 mL three-neck flask to synthesize HEA or multimetallic nanocrystal. Then, 0.1 mmol of four metal precursors and 12 mL of OLAM were added. Metal precursors (Vanadyl(VI) acetylacetonate (VO(acac)$_2$, 99%), iron(III) acetylacetonate (Fe(acac)$_2$, 99+%), cobalt(II) acetylacetonate (Co(acac)$_2$, 99%), and copper(II) acetylacetonate (Cu(acac)$_2$, 98%) were purchased from Acros Organics. Chromium(III) acetylacetonate (Cr(acac)$_3$, 97.5%) and molybdenum(II) acetate dimer (Mo$_2$(OOCCH$_3$)$_4$, 99%) were purchased from Strem. Manganese(II) acetylacetonate (Mn(acac)$_2$) and nickel(II) acetylacetonate (Ni(acac)$_2$, 95%) were purchased from Sigma Aldrich. Zinc(II)

acetylacetonate (Zn(acac)$_2$, 25% Zn) and tungsten(VI) chloride (WCl$_6$, 99.9+%) were purchased from thermo scientific.) were selected according to target metal compositions. The solution was degassed (< 2 Torr) for 10 minutes at 50 °C with stirring of a magnetic stir-bar, and then the temperature was increased to 120 °C. The flask was degassed for an additional 30 minutes. The flask was then backfilled with nitrogen and maintained under a nitrogen atmosphere for the remainder of the synthesis. The flask was heated to 350 °C at a rate of ~20 °C min^{-1} and kept at this temperature for 30 minutes. The flask was cooled under blowing air to 160 °C and then placed in a water bath to cool to room temperature. The nanocrystals were isolated by precipitation using isopropanol and centrifugation (838 rad s^{-1}, 3 minutes). They were then redissolved in 5 mL of toluene. The nanocrystals were washed one more time and kept in toluene for the further use.

Catalyst preparation

The weight loading of Pt/Al$_2$O$_3$ and PtFeCoNiW/Al$_2$O$_3$ was targeted at 0.3 wt. % of Pt. To prepare the catalysts, 3 g of Al$_2$O$_3$, which was prepared by calcining Puralox TH100/150 (Sasol) at 900 °C for 24 hours using heating and cooling ramps of 3 °C min^{-1} in static air, was mixed with 15 mL of ethanol and 135 mL of toluene under vigorous stirring in a round bottom flask. The concentrations of Pt and PtFeCoNiW nanocrystals were measured using the TGA technique described above. Next, an appropriate amount of nanocrystal solution was taken and diluted in toluene with a total volume of 60 mL. The diluted nanocrystal solution was injected into the Al$_2$O solution using a syringe pump with an injection rate of 1.5 mL min^{-1}. After injection, the solution was stirred overnight. Then, nanocrystal/Al$_2$O$_3$ was collected by centrifugation (838 rad s^{-1}, 3 minutes). The clean supernatant after centrifugation indicated the full deposition of nanocrystals on Al$_2$O$_3$. Collected catalysts were dried at 60 °C overnight. Dried catalysts were sieved below 180 µm size. Then, catalysts were treated at 700 °C for 30 seconds to remove ligands from synthesis, as previously reported[59]. Finally, catalysts were sieved again below 180 µm size.

TEM characterization

An unwashed nanocrystal solution was collected and diluted in hexane or toluene to prevent possible oxidation during washing. Nanocrystals were deposited onto TEM grids with 3×3 TEM silicon nitride window array (Norcada) or carbon film 300 mesh grids (Electron Microscopy Sciences), where metal grids were either Au, Cu, or Ni, depending on the nanocrystal compositions using drop-casting. Before measurement, Ar plasma cleaning was done using a plasma cleaner (Model 1020, Fischione instruments) for 60 seconds to remove the organics on nanocrystals. For powder samples, powders were deposited on the Au-carbon film girds by stirring.

Bright-field transmission electron microscopy (TEM) images were collected using an FEI Titan ETEM instrument at 300 kV equipped with a monochromator, an aberration corrector in the image-forming objective lens, and an FEI Tecnai at 200 kV.

High-angle annular dark-field scanning transmission electron microscopy (HAADF-STEM) images and energy dispersive X-ray spectroscopy (EDS maps) maps in Figure 1e, Figure 2h,

Figure 3h, and Figures S9a-b were acquired using an FEI TitanX equipped with SuperEDS detector at 300 kV at the National Center for Electron Microscopy (NCEM) at the Lawrence Berkeley National Laboratory (LBNL). Map acquisition was typically 5~10 minutes at a beam current of 330 pA. Bruker Esprit 1.9 software was used to process and quantify the EDS maps using the following approach. First, a fit of the Bremsstrahlung background X-rays was subtracted from the hyperspectral images using pre-defined fitting regions where no characteristic X-ray peaks appeared. Corrections for escape peaks, pileup peaks, shelf, tail, and shift errors were applied.

HAADF-STEM and EDS maps in Figures 2e-g, Figures 3d and 3i, Figures 4b, 4d, and 4f, Figure S3a, Figure S4a, Figure S9c, Figure S10, Figure S14, Figure S23 were collected using a Thermo Fisher Spectra 300 double-corrected TEM at 300 kV. Map acquisition was typically 5~10 minutes at a beam current of 330 pA. HAAD-STEM was collected with a beam current of 100 pA. The elemental quantification was done by using Velox software.

HAADF-STEM and EDS maps in Figure 5 were collected simultaneously at 100 kV using a TESCAN TENSOR located at the TESCAN demo facility in Tempe, Arizona. Map acquisition was 10 minutes at a beam current of 500 pA.

The EDS maps in Figures 5e and g were analyzed using custom Matlab code to measure the composition profiles shown in Figures 5f and h. First, we estimated the approximate nanoparticle positions from the HAADF signals for all scanned regions. Next, we refined these peak positions (x_0,y_0) over the coordinates (x,y) and the nanoparticle shapes using nonlinear least squares applied to the sum of all EDS maps. We used a fitting function for the intensity I given by an elliptic Gaussian distribution on a background plane:

$$I = I_{peak} \exp[-a(x - x_0)^2 - b(x - x_0)(y - y_0) - c(y - y_0)^2] + I_0 + I_x(x - x_0) + I_y(y - y_0)$$

Where I_{peak} is the peak intensity, (I_0, I_x, I_y) are the background fitting coefficients, and the Gaussian distribution shape is defined by the ellipse parameters (a,b,c). Note that we recover the conventional 2D Gaussian distribution with a standard deviation s when $b = 0$ and $a = c = 1/(2s^2)$. Finally, we estimated a shape-independent composition of each nanoparticle by generating positional bins from the angle-dependent standard deviation for each nanoparticle, summing up the EDS counts of each element inside each bin, and then subtracting an estimated background signal given by the mean EDS intensity of an annular bin from 2.5 standard deviations to 2.5 standard deviations plus 16 pixels. Figures 5f and h plot the mean compositions, given by the average EDS signal from all particles and then normalized to 100% total composition.

X-ray diffraction

The thin layer of nanocrystals was prepared by drop casting the nanocrystals solution on a pre-heated glass slide to obtain a thin layer of nanocrystals. X-ray diffraction measurements were performed using a PANalytical Empyrean diffractometer with Cu Kα radiation (wavelength

1.54059 Å) with a scan rate of 0.05 $^{\circ}s^{-1}$ and a step size of 0.04 $^{\circ}$. The incident X-ray beam was shaped using the iCore automatic incident beam optics and the diffracted intensities were collected using GaliPIX3D FASS X-ray (Non-ambient RRI) detector set up in the 1D scanning mode.

Catalytic characterization

CO oxidation was performed at atmospheric pressure in a custom-built U-tube quartz reactor. The 30 mg of catalyst and 170 mg of Al_2O_3 as a diluent were physically mixed to form the catalyst bed. The catalyst bed was placed between two layers of granular acid-washed quartz in the U-tube reactor, and a k-type thermocouple was placed directly inside the catalyst bed. Micromeritics Eurotherm 2416 furnace was used to heat a reactor. Online gas chromatography (GC) (Buck Scientific Model 910), equipped with a flame ionization detector (FID) with a methanizer and a thermal conductivity detector (TCD), was used to analyze reactants and products.

To remove any absorbed species on the surface, the catalyst was pretreated at 50 mL min^{-1} of 5% O_2/Ar at 300 °C for 30 minutes before the reaction. After pre-treatment, the catalyst was cooled to the initial reaction temperature under Ar flow, and then the reaction mixture of 50 mL min^{-1} 0.4% CO and 4% O_2 (balance Ar) was introduced. Kinetic rates were measured at a steady state, where the CO_2 production was stabilized. Rates were collected at five different temperatures and CO conversion was kept below 10% conversion.

Catalyst aging

The catalyst was aged at atmospheric pressure in a custom-built quartz tube with a tube furnace (MTI Corporation). The crucible with the catalyst was placed in the center of the quartz tube. Then, the gas mixture of 50 mL min^{-1} 4.85% O_2 and 3.13% H_2O (balance Ar) was introduced. The concentration of H_2O was introduced by flowing gas through a saturator filled with Milli-Q water at room temperature. The temperature was raised to the final aging temperature (600 or 650 °C) at 10 °C min^{-1} and stayed at the final temperature for 6 h. Then, the catalyst was cooled down to room temperature under the flow of the same gas mixture.

CO chemisorption

CO chemisorption experiments were performed using a home-built rapid transient flow reactor that has been described previously[90]. Powder catalyst samples and SiC were sieved to 220-300 µm. Catalyst was diluted in four-fold the volumetric amount of SiC and loaded into the microreactor with a bed height of approximately 14.5 mm. The microreactor was then filled to approximately 45 mm with more SiC.

Before each experiment, samples were exposed to 5% O_2/Ar (6.25 sccm O_2/Ar, 18.75 sccm Ar) while heating from room temperature to 300 °C at 20 °C min^{-1} and while held at 300 °C for 30 minutes. Then samples were cooled to 30 °C in Ar (25 sccm) at 20 °C min^{-1}. During CO chemisorption experiments, samples were held at °30 C in Ar (25 sccm) for 30 seconds, switched to a stream of 0.4% CO (0.5 sccm 20% CO/Ar, 24.5 sccm 1% Kr/Ar) via a microelectric valve and

held for 30 seconds, then switched back to the original Ar stream for 30 seconds. The experiment was repeated at least three times per catalyst. The microreactor environment is sampled via a capillary connected to an ultra-high vacuum system with a mass spectrometer capable of sampling at a rate of 250 Hz.

The total amount of CO adsorbed on the catalyst was calculated using the measured differences in normalized CO and Kr signals and their known volumetric flow rates. CO and Kr signal breakthrough curves were fit using a Gompertz function. CO uptake values were adjusted to reflect the measured proportion of CO in the reactor stream, which varied slightly between experiments.

CO-DRIFTS

DRIFTS measurements were obtained using a Harrick Praying Mantis Low Volume High Temperature Reaction Chamber (LV-HVC) reactor cell mounted inside a Fourier-transform infrared spectrometer (FTIR, Bruker INVENIO-R) using the Harrick Praying Mantis diffuse reflectance accessory. The FTIR detector (HgCdTe MCT) was cooled with liquid nitrogen prior to use. The FTIR and Praying Mantis accessory were purged with dry air (5 L min^{-1}) supplied by a purge gas generator (Parker Spectra 15) and gas purifier (Drierite L68GP). The sample cup in the DRIFT cell was heated via the Harrick ATK Temperature Controller, measured with a thermocouple at the bottom of the cup. Because there is a temperature gradient across the z axis of the cup, an optical pyrometer was used to produce a calibration curve for the surface of the catalyst loaded into the cup, and reported temperatures are calibrated values. The sample cup was prepared by inserting a 250-mesh stainless steel disc into the bottom of the cup, then loading the cup with SiC (sieved between 50 and 70 mesh) up to approx. 1 mm from the top, then loading catalyst powder (sieved between 50 and 70 mesh) in a uniform thin layer. Approximately 15 mg of each catalyst was loaded per experiment. After loading the sample cup and installing the cell in the spectrometer, the catalyst was exposed to a stream of 5% O_2 in Ar at a flow rate of 25 mL min^{-1} and, heated to 300 ºC at a rate of 20 ºC min^{-1} and then held for 30 minutes. The catalyst was then cooled to 30 ºC at a rate of 20 ºC min^{-1} under Ar, at which point DRIFT background spectra were recorded. The catalyst was then exposed to a 0.4% CO in Ar stream at a flow rate of 25 mL min^{-1} at which point CO-DRIFT spectra were recorded. Spectra were recorded every 30 seconds and each contain 500 scans with 4 cm^{-1} resolution. Gas phase CO peaks were subtracted using a blank experiment over the support powder (Figure S18).

XAS Experiments

In situ XAS experiment was conducted at the QAS beamline (7-BM), NSLS-II, located at Brookhaven National Laboratory (BNL). Before the experiment, the sample was pelletized and placed in the Nashner-Adler (NA) cell[91]. A thermocouple was positioned near the sample within the NA cell and connected to a temperature controller. Data was collected at Fe K-edge, Co K-edge, Ni K-edge, W L$_3$ edge and Pt L$_2$ edge. A Co filter was used to minimize the elastic scattering effect during Ni K edge measurements. To ensure high-quality data, 30 scans were collected for each edge. The data was collected at room temperature and was analyzed using the Demeter

package[92]. For data analysis, atomic ratio of elements that quantified by EDS in Figure 1e was used.

Computational details

To explore the phase stability of HEAs, we performed high-throughput screening to predict the atomic-scale segregation propensity in their bulk structures. We adopted recent methods and protocols[93,94], which integrates a novel machine learning interatomic potential (MLIP) with replica exchange molecular dynamics and Monte Carlo-based atom swaps (REMD/MC) simulations as implemented in i-Pi[95]. The MLIP, trained on a HEA dataset consisting of 25 transition metals, leverages an alchemical smooth overlap of atomic positions (SOAP)[96] descriptor-based encoding. Subsequent SRO analysis of bulk HEA segregation trends revealed strong alignment with experimental data, validating the model's predictive capability for shortlisting HEA composition with good thermodynamic phase stability[97,98]. Specifically, the Cowley's SRO parameter of an A-B atom pair is calculated by

$$\alpha_{AB}^{(r)} = 1 - \frac{P_{AB}^{(r)}}{2c_A c_B}$$

where $P_{AB}^{(r)}$ is the probability of finding atom-pair A-B at distance *r*, c_A and c_B are the concentrations of species A and B in the alloy.

For the REMD/MC simulations, we used 10 replicas with temperatures logarithmically distributed between 500 K and 933 K. Each bulk system was simulated for 200,000 steps (3 fs timestep) for bulk and is governed by a Langevin thermostat. All bulk structures are of the FCC crystal structure and consists of 256 atoms, while the lattice constants are determined by the experimental values of the constituting metals using the Vegard's law[45].

Acknowledgements

Sciences, of the U.S. Department of Energy under Contract No. DE-AC02-05CH11231. Part of this work was performed at the Stanford Nano Shared Facilities (SNSF) RRID:SCR_023230, supported by the National Science Foundation under award ECCS-2026822. We acknowledge discussions and support from Dr. Maximillian Springer (BASF), and Prof. Michele Ceriotti group (EPFL), specifically Arslan Mazitov, Dr. Nataliya Lopanitsyna, and Dr. Guillaume Fraux, in developing the early prototype of the simulation workflow, and from Roel Sanchez-Carrera (BASF), Fabian Seeler (BASF) and Matthew T. Caudle (BASF) on the synthesis and catalytic experiments.

Competing interests

J.O., E.G., S.H., S.D., M.C., and C.L.-P. are listed as inventors on US patent application 2024/052936 related to this work. All other coauthors declare no competing interests.

References

1. Tao, A. R., Habas, S. & Yang, P. Shape control of colloidal metal nanocrystals. *Small* **4**, 310–325 (2008).

2. Losch, P., Huang, W., Goodman, E. D., Wrasman, C. J., Holm, A., Riscoe, A. R., Schwalbe, J. A. & Cargnello, M. Colloidal nanocrystals for heterogeneous catalysis. *Nano Today* **24**, 15–47 (2019).

3. Guntern, Y. T., Okatenko, V., Pankhurst, J., Varandili, S. B., Iyengar, P., Koolen, C., Stoian, D., Vavra, J. & Buonsanti, R. Colloidal Nanocrystals as Electrocatalysts with Tunable Activity and Selectivity. *ACS Catal.* **11**, 1248–1295 (2021).

4. Chen, C. J., Oh, J., Yang, A. C., Zhou, C., Liccardo, G., Sapru, S. & Cargnello, M. Understanding the effects of manganese and zinc promoters on ferrite catalysts for CO2 hydrogenation to hydrocarbons through colloidal nanocrystals. *Surf. Sci.* **741**, (2024).

5. Loiudice, A., Lobaccaro, P., Kamali, E. A., Thao, T., Huang, B. H., Ager, J. W. & Buonsanti, R. Tailoring Copper Nanocrystals towards C2 Products in Electrochemical CO2 Reduction. *Angew. Chemie - Int. Ed.* **55**, 5789–5792 (2016).

6. Grim, J. Q., Manna, L. & Moreels, I. A sustainable future for photonic colloidal nanocrystals. *Chem. Soc. Rev.* **44**, 5897–5914 (2015).

7. Shirasaki, Y., Supran, G. J., Bawendi, M. G. & Bulović, V. Emergence of colloidal quantum-dot light-emitting technologies. *Nat. Photonics* **7**, 13–23 (2013).

8. Talapin, D. V. & Murray, C. B. Applied physics: PbSe nanocrystal solids for n- and p-channel thin film field-effect transistors. *Science (80-.).* **310**, 86–89 (2005).

9. Kagan, C. R. & Murray, C. B. Charge transport in strongly coupled quantum dot solids. *Nat. Nanotechnol.* **10**, 1013–1026 (2015).

10. Talapin, D. V., Lee, J. S., Kovalenko, M. V. & Shevchenko, E. V. Prospects of colloidal nanocrystals for electronic and optoelectronic applications. *Chem. Rev.* **110**, 389–458 (2010).

11. Buonsanti, R., Llordes, A., Aloni, S., Helms, B. A. & Milliron, D. J. Tunable infrared absorption and visible transparency of colloidal aluminum-doped zinc oxide nanocrystals. *Nano Lett.* **11**, 4706–4710 (2011).

12. Buonsanti, R. & Cossairt, B. The Future of Colloidal Semiconductor Nanocrystals. *Chem. Mater.* **37**, 1333–1334 (2025).

13. Kwon, H. J., Shin, K., Soh, M., Chang, H., Kim, J., Lee, J., Ko, G., Kim, B. H., Kim, D. & Hyeon, T. Large-Scale Synthesis and Medical Applications of Uniform-Sized Metal Oxide Nanoparticles. *Adv. Mater.* **30**, 1–24 (2018).

14. Mitchell, M. J., Billingsley, M. M., Haley, R. M., Wechsler, M. E., Peppas, N. A. & Langer, R. Engineering precision nanoparticles for drug delivery. *Nat. Rev. Drug Discov.* **20**, 101–124 (2021).

15. Jain, P. K., Huang, X., El-Sayed, I. H. & El-Sayed, M. A. Noble metals on the nanoscale: Optical and photothermal properties and some applications in imaging, sensing, biology, and medicine. *Acc. Chem. Res.* **41**, 1578–1586 (2008).

16. Xu, C., Xie, J., Ho, D., Wang, C., Kohler, N., Walsh, E. G., Morgan, J. R., Chin, Y. E. & Sun, S. Au-Fe3O4 dumbbell nanoparticles as dual-functional. *Angew. Chemie - Int. Ed.* **47**, 173–176 (2008).

17. Kim, D., Kim, J., Park, Y. Il, Lee, N. & Hyeon, T. Recent Development of Inorganic Nanoparticles for Biomedical Imaging. *ACS Cent. Sci.* **4**, 324–336 (2018).

18. Alivisatos, P. The use of nanocrystals in biological detection. *Nat. Biotechnol.* **22**, 47–52 (2004).

19. Niu, G., Ruditskiy, A., Vara, M. & Xia, Y. Toward continuous and scalable production of colloidal nanocrystals by switching from batch to droplet reactors. *Chem. Soc. Rev.* **44**, 5806–5820 (2015).

20. Kovalenko, M. V., Manna, L., Cabot, A., Hens, Z., Talapin, D. V., Kagan, C. R., Klimov, V. I., Rogach, A. L., Reiss, P., Milliron, D. J., Guyot-Sionnnest, P., Konstantatos, G., Parak, W. J., Hyeon, T., Korgel, B. A., Murray, C. B. & Heiss, W. Prospects of nanoscience with nanocrystals. *ACS Nano* **9**, 1012–1057 (2015).

21. Wang, Y., Kumar, A., Wu, T. Y. & Weiss, D. S. Single-qubit gates based on targeted phase shifts in a 3D neutral atom array. *Science (80-.).* **352**, 1562–1565 (2016).

22. Koo, W. T., Millstone, J. E., Weiss, P. S. & Kim, I. D. The Design and Science of Polyelemental Nanoparticles. *ACS Nano* vol. 14 6407–6413 at https://doi.org/10.1021/acsnano.0c03993 (2020).

23. Yao, Y., Dong, Q., Brozena, A., Luo, J., Miao, J., Chi, M., Wang, C., Kevrekidis, I. G., Ren, Z. J., Greeley, J., Wang, G., Anapolsky, A. & Hu, L. High-entropy nanoparticles: Synthesis-structureproperty relationships and data-driven discovery. *Science* vol. 376 at https://doi.org/10.1126/science.abn3103 (2022).

24. Bondesgaard, M., Broge, N. L. N., Mamakhel, A., Bremholm, M. & Iversen, B. B. General Solvothermal Synthesis Method for Complete Solubility Range Bimetallic and High-Entropy Alloy Nanocatalysts. *Adv. Funct. Mater.* **29**, (2019).

25. Yao, Y., Huang, Z., Xie, P., Lacey, S. D., Jacob, R. J., Xie, H., Chen, F., Nie, A., Pu, T., Rehwoldt, M., Yu, D., Zachariah, M. R., Wang, C., Shahbazian-Yassar, R., Li, J. & Hu, L. *Carbothermal Shock Synthesis of High-Entropy-Alloy Nanoparticles*. *Science* vol. 359 http://science.sciencemag.org/ (2018).

26. Kim, H., Yoo, T. Y., Bootharaju, M. S., Kim, J. H., Chung, D. Y. & Hyeon, T. Noble Metal-Based Multimetallic Nanoparticles for Electrocatalytic Applications. *Advanced Science* vol. 9 at https://doi.org/10.1002/advs.202104054 (2022).

27. Wu, D., Kusada, K., Nanba, Y., Koyama, M., Yamamoto, T., Toriyama, T., Matsumura, S., Seo, O., Gueye, I., Kim, J., Rosantha Kumara, L. S., Sakata, O., Kawaguchi, S., Kubota, Y. & Kitagawa, H. Noble-Metal High-Entropy-Alloy Nanoparticles: Atomic-Level Insight into the Electronic Structure. *J. Am. Chem. Soc.* **144**, 3365–3369 (2022).

28. Cao, G., Liang, J., Guo, Z., Yang, K., Wang, G., Wang, H., Wan, X., Li, Z., Bai, Y., Zhang, Y., Liu, J., Feng, Y., Zheng, Z., Lu, C., He, G., Xiong, Z., Liu, Z., Chen, S., Guo, Y., *et al.* Liquid metal for high-entropy alloy nanoparticles synthesis. *Nature* (2023) doi:10.1038/s41586-023-06082-9.

29. Chen, Y., Zhan, X., Bueno, S. L. A., Shafei, I. H., Ashberry, H. M., Chatterjee, K., Xu, L., Tang, Y. & Skrabalak, S. E. Synthesis of monodisperse high entropy alloy nanocatalysts from core@shell nanoparticles. *Nanoscale Horizons* **6**, 231–237 (2021).

30. Xie, P., Yao, Y., Huang, Z., Liu, Z., Zhang, J., Li, T., Wang, G., Shahbazian-Yassar, R., Hu, L. & Wang, C. Highly efficient decomposition of ammonia using high-entropy alloy catalysts. *Nat. Commun.* **10**, (2019).

31. Gao, S., Hao, S., Huang, Z., Yuan, Y., Han, S., Lei, L., Zhang, X., Shahbazian-Yassar, R. & Lu, J. Synthesis of high-entropy alloy nanoparticles on supports by the fast moving bed pyrolysis. *Nat. Commun.* **11**, (2020).

32. Ye, Y. F., Wang, Q., Lu, J., Liu, C. T. & Yang, Y. High-entropy alloy: challenges and prospects. *Materials Today* vol. 19 349–362 at https://doi.org/10.1016/j.mattod.2015.11.026 (2016).

33. Dey, G. R., Soliman, S. S., McCormick, C. R., Wood, C. H., Katzbaer, R. R. & Schaak, R. E. Colloidal Nanoparticles of High Entropy Materials: Capabilities, Challenges, and Opportunities in Synthesis and Characterization. *ACS Nanoscience Au* vol. 4 3–20 at https://doi.org/10.1021/acsnanoscienceau.3c00049 (2024).

34. Moreira Da Silva, C., Amara, H., Fossard, F., Girard, A., Loiseau, A. & Huc, V. Colloidal synthesis of nanoparticles: from bimetallic to high entropy alloys. *Nanoscale* **14**, 9832–9841 (2022).

35. Dey, G. R., McCormick, C. R., Soliman, S. S., Darling, A. J. & Schaak, R. E. Chemical Insights into the Formation of Colloidal High Entropy Alloy Nanoparticles. *ACS Nano* **17**, 5943–5955 (2023).

36. Dey, G. R., Young, H. L., Teklu, S., Soliman, S. S. & Schaak, R. E. Influence of Nanoparticle Seeds on the Formation and Growth of High Entropy Alloys during Core@Shell Nanoparticle Synthesis. *ACS Nano* (2025) doi:10.1021/acsnano.4c16417.

37. Toshima, N. & Yonezawa, T. Bimetallic nanoparticles - Novel materials for chemical and physical applications. *New J. Chem.* **22**, 1179–1201 (1998).

38. Xia, X., Wang, Y., Ruditskiy, A. & Xia, Y. 25th anniversary article: Galvanic replacement: A simple and versatile route to hollow nanostructures with tunable and well-controlled properties. *Adv. Mater.* **25**, 6313–6333 (2013).

39. Broge, N. L. N., Bondesgaard, M., Søndergaard-Pedersen, F., Roelsgaard, M. & Iversen, B. B. Autocatalytic Formation of High-Entropy Alloy Nanoparticles. *Angew. Chemie - Int. Ed.* **59**, 21920–21924 (2020).

40. Bueno, S. L. A., Leonardi, A., Kar, N., Chatterjee, K., Zhan, X., Chen, C., Wang, Z., Engel, M., Fung, V. & Skrabalak, S. E. Quinary, Senary, and Septenary High Entropy Alloy Nanoparticle Catalysts from Core@Shell Nanoparticles and the Significance of

Intraparticle Heterogeneity. *ACS Nano* **16**, 18873–18885 (2022).

41. Kar, N., McCoy, M., Wolfe, J., Bueno, S. L. A., Shafei, I. H. & Skrabalak, S. E. Retrosynthetic design of core–shell nanoparticles for thermal conversion to monodisperse high-entropy alloy nanoparticles. *Nat. Synth.* **3**, 175–184 (2024).

42. Cowley, J. M. An approximate theory of order in alloys. *Phys. Rev.* **77**, 669–675 (1950).

43. Li, Y., Lin, H., Zhou, W., Sun, L., Samanta, D. & Mirkin, C. A. *Corner-, Edge-, and Facet-Controlled Growth of Nanocrystals*. https://www.science.org (2021).

44. Yang, T. H., Zhou, S., Gilroy, K. D., Figueroa-Cosme, L., Lee, Y. H., Wu, J. M. & Xia, Y. Autocatalytic surface reduction and its role in controlling seed-mediated growth of colloidal metal nanocrystals. *Proc. Natl. Acad. Sci. U. S. A.* **114**, 13619–13624 (2017).

45. Vegard, L. Die Konstitution der Mischkristalle und die Raumfüllung der Atome. *Zeitschrift für Phys.* **5**, 17–26 (1921).

46. Chen, P. C., Gao, M., McCandler, C. A., Song, C., Jin, J., Yang, Y., Maulana, A. L., Persson, K. A. & Yang, P. Complete miscibility of immiscible elements at the nanometre scale. *Nat. Nanotechnol.* **19**, 775–781 (2024).

47. Xiong, S., Qi, W., Huang, B. & Wang, M. Size-, shape- and composition-dependent alloying ability of bimetallic nanoparticles. *ChemPhysChem* **12**, 1317–1324 (2011).

48. Gamler, J. T. L., Leonardi, A., Sang, X., Koczkur, K. M., Unocic, R. R., Engel, M. & Skrabalak, S. E. Effect of lattice mismatch and shell thickness on strain in core@shell nanocrystals. *Nanoscale Adv.* **2**, 1105–1114 (2020).

49. Smith, A. M., Mohs, A. M. & Nie, S. Tuning the optical and electronic properties of colloidal nanocrystals by lattice strain. *Nat. Nanotechnol.* **4**, 56–63 (2009).

50. Sneed, B. T., Young, A. P. & Tsung, C. K. Building up strain in colloidal metal nanoparticle catalysts. *Nanoscale* **7**, 12248–12265 (2015).

51. Jin, M., Zhang, H., Wang, J., Zhong, X., Lu, N., Li, Z., Xie, Z., Kim, M. J. & Xia, Y. Copper can still be epitaxially deposited on palladium nanocrystals to generate core-shell nanocubes despite their large lattice mismatch. *ACS Nano* **6**, 2566–2573 (2012).

52. Zeng, J., Zhu, C., Tao, J., Jin, M., Zhang, H., Li, Z. Y., Zhu, Y. & Xia, Y. Controlling the nucleation and growth of silver on palladium nanocubes by manipulating the reaction kinetics. *Angew. Chemie - Int. Ed.* **51**, 2354–2358 (2012).

53. Xia, Y., Gilroy, K. D., Peng, H. & Xia, X. Seed-Mediated Growth of Colloidal Metal Nanocrystals. *Angew. Chemie* **129**, 60–98 (2017).

54. Shibata, T., Bunker, B. A., Zhang, Z., Meisel, D., Vardeman, C. F. & Gezelter, J. D. Size-dependent spontaneous alloying of Au-Ag nanoparticles. *J. Am. Chem. Soc.* **124**, 11989–11996 (2002).

55. Olshin, P. K., Sheardy, A. T., Zhukovskyi, M. A. & Mukasyan, A. S. On the Atomic Scale Diffusion in Au-Ag Nanoparticles. *J. Phys. Chem. C* **128**, 4079–4085 (2024).

56. Maulana, A. L., Chen, P. C., Shi, Z., Yang, Y., Lizandara-Pueyo, C., Seeler, F., Abruña, H. D., Muller, D., Schierle-Arndt, K. & Yang, P. Understanding the Structural Evolution of IrFeCoNiCu High-Entropy Alloy Nanoparticles under the Acidic Oxygen Evolution Reaction. *Nano Lett.* **23**, 6637–6644 (2023).

57. Chen, Z. W., Li, J., Ou, P., Huang, J. E., Wen, Z., Chen, L. X., Yao, X., Cai, G. M., Yang, C. C., Singh, C. V. & Jiang, Q. Unusual Sabatier principle on high entropy alloy catalysts for hydrogen evolution reactions. *Nat. Commun.* **15**, (2024).

58. Xin, Y., Li, S., Qian, Y., Zhu, W., Yuan, H., Jiang, P., Guo, R. & Wang, L. High-Entropy Alloys as a Platform for Catalysis: Progress, Challenges, and Opportunities. *ACS Catal.* **10**, 11280–11306 (2020).

59. Cargnello, M., Chen, C., Diroll, B. T., Doan-Nguyen, V. V. T., Gorte, R. J. & Murray, C. B. Efficient Removal of Organic Ligands from Supported Nanocrystals by Fast Thermal Annealing Enables Catalytic Studies on Well-Defined Active Phases. *J. Am. Chem. Soc.* **137**, 6906–6911 (2015).

60. Datye, A. K., Xu, Q., Kharas, K. C. & McCarty, J. M. Particle size distributions in heterogeneous catalysts: What do they tell us about the sintering mechanism? in *Catalysis Today* vol. 111 59–67 (2006).

61. Oh, J., Beck, A., Goodman, E. D., Roling, L. T., Boucly, A., Artiglia, L., Abild-Pedersen, F., van Bokhoven, J. A. & Cargnello, M. Colloidally Engineered Pd and Pt Catalysts Distinguish Surface- and Vapor-Mediated Deactivation Mechanisms. *ACS Catal.* **13**, 1812–1822 (2023).

62. Plessow, P. N. & Abild-Pedersen, F. Sintering of Pt Nanoparticles via Volatile PtO2: Simulation and Comparison with Experiments. *ACS Catal.* **6**, 7098–7108 (2016).

63. Aitbekova, A., Zhou, C., Stone, M. L., Lezama-Pacheco, J. S., Yang, A.-C., Hoffman, A. S., Goodman, E. D., Huber, P., Stebbins, J. F., Bustillo, K. C., Ercius, P., Ciston, J., Bare, S. R., Plessow, P. N. & Cargnello, M. Templated encapsulation of platinum-based catalysts promotes high-temperature stability to 1,100 °C. *Nat. Mater.* **21**, 1290–1297 (2022).

64. Porter, S., Ghosh, A., Liu, C. H., Kunwar, D., Thompson, C., Alcala, R., Dean, D. P., Miller, J. T., DeLaRiva, A., Pham, H., Peterson, E., Brearley, A., Watt, J., Kyriakidou, E. A. & Datye, A. K. Biphasic Janus Particles Explain Self-Healing in Pt–Pd Diesel Oxidation Catalysts. *ACS Catal.* **13**, 5456–5471 (2023).

65. Lee, S., Gadelrab, K., Cheng, L., Braaten, J. P., Wu, H. & Ross, F. M. Simultaneous 2D Projection and 3D Topographic Imaging of Gas-Dependent Dynamics of Catalytic Nanoparticles. *ACS Nano* **18**, 21258–21267 (2024).

66. Nie, L., Mei, D., Xiong, H., Peng, B., Ren, Z., Hernandez, X. I. P., DeLaRiva, A., Wang, M., Engelhard, M. H., Kovarik, L., Datye, A. K. & Wang, Y. Activation of surface lattice oxygen in single-atom Pt/CeO 2 for low-temperature CO oxidation. *Science (80-.).* **358**, 1419–1423 (2017).

67. Zhang, Z., Tian, J., Lu, Y., Yang, S., Jiang, D., Huang, W., Li, Y., Hong, J., Hoffman, A.

S., Bare, S. R., Engelhard, M. H., Datye, A. K. & Wang, Y. Memory-dictated dynamics of single-atom Pt on CeO2 for CO oxidation. *Nat. Commun.* **14**, 2664 (2023).

68. Pereira-Hernández, X. I., DeLaRiva, A., Muravev, V., Kunwar, D., Xiong, H., Sudduth, B., Engelhard, M., Kovarik, L., Hensen, E. J. M., Wang, Y. & Datye, A. K. Tuning Pt-CeO2 interactions by high-temperature vapor-phase synthesis for improved reducibility of lattice oxygen. *Nat. Commun.* **10**, 1358 (2019).

69. Kim, T. S., O'Connor, C. R. & Reece, C. Interrogating site dependent kinetics over SiO2-supported Pt nanoparticles. *Nat. Commun.* **15**, 1–12 (2024).

70. Nekrylova, J. V. & Harrison, I. Site resolved adsorption dynamics of CO on Pt(111). *Chem. Phys.* **205**, 37–46 (1996).

71. Kale, M. J. & Christopher, P. Utilizing Quantitative in Situ FTIR Spectroscopy To Identify Well-Coordinated Pt Atoms as the Active Site for CO Oxidation on Al 2 O 3 - Supported Pt Catalysts. *ACS Catal.* **6**, 5599–5609 (2016).

72. Weilach, C., Spiel, C., Föttinger, K. & Rupprechter, G. Carbonate formation on Al2O3 thin film model catalyst supports. *Surf. Sci.* **605**, 1503–1509 (2011).

73. Morfin, F., Dessal, C., Sangnier, A., Chizallet, C. & Piccolo, L. Identification of Stable Species Formed Under CO Adsorption and Oxidation on Alumina-Supported Single Pt Atoms: Why Nanoparticles Are More Active. *ACS Catal.* **14**, 9628–9639 (2024).

74. Zecchina, A., Scarano, D. & Reller, A. Infrared spectra of CO adsorbed on prismatic faces of α-Fe2O3. *J. Chem. Soc. Faraday Trans. 1 Phys. Chem. Condens. Phases* **84**, 2327–2333 (1988).

75. Mehl, S., Ferstl, P., Schuler, M., Toghan, A., Brummel, O., Hammer, L., Schneider, M. A. & Libuda, J. Thermal evolution of cobalt deposits on Co3O4(111): Atomically dispersed cobalt, two-dimensional CoO islands, and metallic Co nanoparticles. *Phys. Chem. Chem. Phys.* **17**, 23538–23546 (2015).

76. Vesecky, S. M., Xu, X. & Goodman, D. W. Infrared study of CO on NiO(100). *J. Vac. Sci. Technol. A Vacuum, Surfaces, Film.* **12**, 2114–2118 (1994).

77. Ivanova, E., Mihaylov, M., Thibault-Starzyk, F., Daturi, M. & Hadjiivanov, K. FTIR spectroscopy study of CO and NO adsorption and co-adsorption on Pt/TiO2. *J. Mol. Catal. A Chem.* **274**, 179–184 (2007).

78. Song, B., Yang, Y., Rabbani, M., Yang, T. T., He, K., Hu, X., Yuan, Y., Ghildiyal, P., Dravid, V. P., Zachariah, M. R., Saidi, W. A., Liu, Y. & Shahbazian-Yassar, R. In situ oxidation studies of high-entropy alloy nanoparticles. *ACS Nano* **14**, 15131–15143 (2020).

79. Cargnello, M., Doan-Nguyen, V. V. T., Gordon, T. R., Diaz, R. E., Stach, E. A., Gorte, R. J., Fornasiero, P. & Murray, C. B. Control of Metal Nanocrystal Size Reveals Metal-Support Interface Role for Ceria Catalysts. *Science (80-.).* **341**, 771–773 (2013).

80. An, K., Alayoglu, S., Musselwhite, N., Plamthottam, S., Melaet, G., Lindeman, A. E. & Somorjai, G. A. Enhanced CO Oxidation Rates at the Interface of Mesoporous Oxides and Pt Nanoparticles. *J. Am. Chem. Soc.* **135**, 16689–16696 (2013).

81. Zhou, C., Oh, J., Stone, M. L., Richardson, S., Chung, P. H., Osio-Norgaard, J., Nhan, B. T., Kumar, A., Chi, M. & Cargnello, M. A General Approach for Metal Nanoparticle Encapsulation Within Porous Oxides. *Adv. Mater.* **2409710**, 1–10 (2024).

82. Bunluesin, T., Putna, E. S. & Gorte, R. J. *A Comparison of CO Oxidation on Ceria-Supported Pt, Pd, and Rh*. *Catalysis Letters* vol. 41 (1996).

83. Goodman, E. D., Carlson, E. Z., Dietze, E. M., Tahsini, N., Johnson, A., Aitbekova, A., Nguyen Taylor, T., Plessow, P. N. & Cargnello, M. Size-controlled nanocrystals reveal spatial dependence and severity of nanoparticle coalescence and Ostwald ripening in sintering phenomena. *Nanoscale* **13**, 930–938 (2021).

84. Cao, A. & Veser, G. Exceptional high-temperature stability through distillation-like self-stabilization in bimetallic nanoparticles. *Nat. Mater.* **9**, 75–81 (2010).

85. Yu, S. W., Kwon, S., Chen, Y., Xie, Z., Lu, X., He, K., Hwang, S., Chen, J. G., Goddard, W. A. & Zhang, S. Construction of a Pt-CeOx Interface for the Electrocatalytic Hydrogen Evolution Reaction. *Adv. Funct. Mater.* **2402966**, (2024).

86. Zhang, J. & Fang, J. A general strategy for preparation of Pt 3d-transition metal (Co, Fe, Ni) nanocubes. *J. Am. Chem. Soc.* **131**, 18543–18547 (2009).

87. Wrasman, C. J., Boubnov, A., Riscoe, A. R., Hoffman, A. S., Bare, S. R. & Cargnello, M. Synthesis of Colloidal Pd/Au Dilute Alloy Nanocrystals and Their Potential for Selective Catalytic Oxidations. *J. Am. Chem. Soc.* **140**, 12930–12939 (2018).

88. Peng, S., Lee, Y., Wang, C., Yin, H., Dai, S. & Sun, S. A facile synthesis of monodisperse Au nanoparticles and their catalysis of CO oxidation. *Nano Res.* **1**, 229–234 (2008).

89. Willis, J. J., Gallo, A., Sokaras, D., Aljama, H., Nowak, S. H., Goodman, E. D., Wu, L., Tassone, C. J., Jaramillo, T. F., Abild-Pedersen, F. & Cargnello, M. Systematic Structure–Property Relationship Studies in Palladium-Catalyzed Methane Complete Combustion. *ACS Catal.* **7**, 7810–7821 (2017).

90. High, E. A., Lee, E. & Reece, C. A transient flow reactor for rapid gas switching at atmospheric pressure. *Rev. Sci. Instrum.* **94**, (2023).

91. Frenkel, A. I., Hills, C. W. & Nuzzo, R. G. A View from the Inside: Complexity in the Atomic Scale Ordering of Supported Metal Nanoparticles. *J. Phys. Chem. B* **105**, 12689–12703 (2001).

92. Ravel, B. & Newville, M. ATHENA, ARTEMIS, HEPHAESTUS: Data analysis for X-ray absorption spectroscopy using IFEFFIT. *J. Synchrotron Radiat.* **12**, 537–541 (2005).

93. Mazitov, A., Springer, M. A., Lopanitsyna, N., Fraux, G., De, S. & Ceriotti, M. Surface segregation in high-entropy alloys from alchemical machine learning. *JPhys Mater.* **7**, (2024).

94. Lopanitsyna, N., Fraux, G., Springer, M. A., De, S. & Ceriotti, M. Modeling high-entropy transition metal alloys with alchemical compression. *Phys. Rev. Mater.* **7**, 1–15 (2023).

95. Kapil, V., Rossi, M., Marsalek, O., Petraglia, R., Litman, Y., Spura, T., Cheng, B.,

Cuzzocrea, A., Meißner, R. H., Wilkins, D. M., Helfrecht, B. A., Juda, P., Bienvenue, S. P., Fang, W., Kessler, J., Poltavsky, I., Vandenbrande, S., Wieme, J., Corminboeuf, C., *et al.* i-PI 2.0: A universal force engine for advanced molecular simulations. *Comput. Phys. Commun.* **236**, 214–223 (2019).

96. De, S., Bartók, A. P., Csányi, G. & Ceriotti, M. Comparing molecules and solids across structural and alchemical space. *Phys. Chem. Chem. Phys.* **18**, 13754–13769 (2016).

97. Batchelor, T. A. A., Pedersen, J. K., Winther, S. H., Castelli, I. E., Jacobsen, K. W. & Rossmeisl, J. High-Entropy Alloys as a Discovery Platform for Electrocatalysis. *Joule* **3**, 834–845 (2019).

98. Li, Y. & Guo, W. Machine-learning model for predicting phase formations of high-entropy alloys. *Phys. Rev. Mater.* **3**, 95005 (2019).